GFZ

Helmholtz-Zentrum
POTSDAM

HELMHOLTZ-ZENTRUM POTSDAM
DEUTSCHES
GEOFORSCHUNGSZENTRUM

H. Dobslaw, I. Bergmann–Wolf, R. Dill, E. Forootan,
V. Klemann, J. Kusche, I. Sasgen

Updating ESA's Earth System Model for Gravity Mission Simulation Studies

1. Model Description and Validation

Scientific Technical Report STR14/07

www.gfz-potsdam.de

HELMHOLTZ
GEMEINSCHAFT

Recommended citation:

Dobslaw, H., Bergmann-Wolf, I., Dill, R., Forootan, E., Klemann, V., Kusche, J., Sasgen, I. (2014), Updating ESA's Earth System Model for Gravity Mission Simulation Studies: 1. Model Description and Validation. *Scientific Technical Report 14/07, GFZ German Research Centre for Geosciences*. doi: 10.2312/GFZ.b103-14079.

Imprint

Helmholtz Centre Potsdam
GFZ German Research Centre for Geosciences

Telegrafenberg
D-14473 Potsdam

Published in Potsdam, Germany
August 2014

ISSN 1610-0956

DOI: 10.2312/GFZ.b103-14079
URN: urn:nbn:de:kobv:b103-14079

This work is published in the GFZ series
Scientific Technical Report (STR)
and electronically available at GFZ website
www.gfz-potsdam.de

ESA Contract No. 4000109421

Updating ESA's Earth System Model for Gravity Mission Simulation Studies

1. Model Description and Validation

Doc. No.: ESAESM_ND1_i1r2
Issue: 1
Revision: 2
Date: August 5, 2014
Authors: H. Dobslaw, I. Bergmann–Wolf, R. Dill, E. Forootan, V. Klemann, J. Kusche, I. Sasgen
ESA TO: R. Haagmans (ESTEC)

GFZ Potsdam, Department Geodesy and Remote Sensing

Scientific Technical Report STR 14/07
DOI: 10.2312/GFZ.b103-14079

ESA Study Contract Report

ESA Contract No.	Subject		Contractor
4000109421	Updating ESA's Earth System Model for Gravity Mission Simulation Studies		GFZ German Research Centre for Geosciences
ESA CR No.	**STAR CODE**	**No. of Volumes:** 3 **This is Volume No.** 1	**Contractors Reference**

Abstract

The ability of any satellite gravity mission concept to monitor mass transport processes in the Earth system is typically tested well ahead of its implementation by means of various simulation studies. Those studies often extend from the simulation of realistic orbits and instrumental data all the way down to the retrieval of global gravity field solution time-series. Basic requirement for all these simulations are realistic representations of the spatio-temporal mass variability in the different sub-systems of the Earth, as a source model for the orbit computations.

For such simulations, a suitable source model is required to represent (i) high-frequency (i.e., sub-daily to weekly) mass variability in the atmosphere and oceans, in order to realistically include the effects of temporal aliasing due to non-tidal high-frequency mass variability into the retrieved gravity fields. In parallel, (ii) low-frequency (i.e., monthly to interannual) variability needs to be modelled with realistic amplitudes, particularly at small spatial scales, in order to assess to what extent a new mission concept might provide further insight into physical processes currently not observable.

The new source model documented here attempts to fulfil both requirements: Based on ECMWF's recent atmospheric reanalysis ERA-Interim and corresponding simulations from numerical models of the other Earth system components, it offers spherical harmonic coefficients of the time-variable global gravity field due to mass variability in atmosphere, oceans, the terrestrial hydrosphere including the ice-sheets and glaciers, as well as the solid Earth. Simulated features range from sub-daily to multiyear periods with a spatial resolution of spherical harmonics degree and order 180 over a period of 12 years. In addition to the source model, a de-aliasing model for atmospheric and oceanic high-frequency variability with augmented systematic and random noise is required for a realistic simulation of the gravity field retrieval process, whose necessary error characteristics are discussed.

The documentation is organized as follows: The characteristics of the updated ESM along with some basic validation are presented in Volume 1 of this report (Dobslaw *et al.*, 2014). A detailed comparison to the original ESA ESM (Gruber *et al.*, 2011) is provided in Volume 2 (Bergmann-Wolf *et al.*, 2014a), while Volume 3 (Forootan *et al.*, 2014) contains a description of the strategy to derive a realistically noisy de-aliasing model for the high-frequency mass variability in atmosphere and oceans.

The files of the updated ESA Earth System Model for gravity mission simulation studies are accessible at DOI:10.5880/GFZ.1.3.2014.001.

The work described in this report was performed under an ESA contract. Responsibility for the content resides in the author or organization that prepared it.

Authors:
H. Dobslaw, I. Bergmann–Wolf, R. Dill, E. Forootan, V. Klemann, J. Kusche, I. Sasgen

Name of ESA Study Manager	ESA Budget Heading
Roger Haagmans Section: Earth Surfaces and Interior Section Division: Mission Science Division Department: Science, Application and Future Technologies	

Scientific Technical Report STR 14/07
DOI: 10.2312/GFZ.b103-14079

Contents

List of Tables

Scientific Technical Report STR 14/07
DOI: 10.2312/GFZ.b103-14079

List of Figures

List of Acronyms

A	atmospheric component of the updated ESM including modified IB-correction
Ac	atmospheric component of the updated ESM with blended high-resolution data from COSMO-EU over Europe
AcOHIS	sum of the respective five components of the updated ESM
AnoIB	atmospheric component of the updated ESM without modified IB-correction
AOD1B	GRACE Atmosphere and Ocean De-aliasing Level-1B product
AOHIS	sum of the respective five components of the updated ESM
CE system	reference system originating at redistribution of earth's internal masses
CF system	reference system originating at surface displacement
CM system	reference sysyem originating of total mass distribution in the earth
COSMO-EU	Regional weather forecast model of German Weather Service
DAHITI	Database for Hydrological Time Series of Inland Waters
DDK[235]	different versions of the anisotropic GRACE filter of (Kusche, 2007)
ECMWF	European Centre for Medium-Range Weather Forecasts
Envisat	Environmental Satellite of ESA; Satellite Radar Altimetry Mission
EOF	Empirical Orthogonal Function
ERA-Interim	most recent global atmospheric re-analysis of ECMWF (1979 - 2014)
ESA	European Space Agency
ESM	Earth System Model
GAC	monthly mean of the atmospheric and oceanic masses that are reduced during de-aliasing procedure applied in the GRACE gravity field retrieval process
GIA	Glacial Isostatic Adjustment
GPS	Global Positioning System
GRACE	Gravity Recovery And Climate Experiment
GSM	global gravity model from GRACE with atmospheric and oceanic effects removed
H	terrestrial hydrosphere component of the updated ESM
HOPE	Hamburg Ocean Primitive Equation Model
I	cryosphere component of the updated ESM
IB-Correction	Inverted Barometric Correction
ICESat	Ice, Cloud and Land Elevation Satellite
ITG3D	Atmospheric de-aliasing product based on ERA-Interim by Univ. Bonn
LSDM	Land Surface Discharge Model
MPIOM	Max-Planck-Institute for Meteorology Ocean Model
O	ocean component of the updated ESM
OMCT	Ocean Model for Circulation and Tides
PCA	Principal Component Analysis
PREM	Preliminary Reference Earth Model
RACMO2/ANT	Regional Climate Model for Antarctica

RACMO2/GR	Regional Climate Model for Greenland
REGINA	name of an ESA Support to Science Element project
RL05	Release Number 05
S	solid earth component of the updated ESM
S1(p)	diurnal air tide
S2(p)	semidiurnal air tide
SLR	Satellite Laser Ranging
STORM	German consortium for the development of a very high resolution climate model
STSE	Support to Science Element of ESA
TWS	Terrestrial Water Storage
UTC	Universal Time Coordinated

Chapter 1

Introduction

The realistic assessment of candidate constellations for a future satellite gravity mission dedicated to the observation of large-scale mass transport phenomena requires extensive end-to-end simulations: starting from simulated orbits based on a realistic global model of large-scale mass redistributions that cause time-changes in the gravity field all the way down to the retrieval of global gravity field solutions and the application of appropriate post-processing techniques to remove spatially anisotropic errors. Critically important prerequisites for such simulations are (i) a model of the time-variable gravity field of the Earth that contains realistic variability on a wide range of spatial and temporal scales important for satellite gravimetry, and (ii) realistically noisy background models for the gravity field retrieval process to cope with high-frequency mass variability that otherwise aliases into the time-mean gravity fields. Those background models are to be derived from the source models by augmenting them with realistic errors that are correlated in time and space.

Within this report, a new time-variable gravity field model for satellite gravity studies is documented that covers a full solar cycle of 12 years with both high spatial (maximum spherical harmonic degree and order is 180) and temporal (time sampling is 6 hours) resolution, and includes the most important mass transport processes at, above, and below the Earth surface on a wide range of time-scales.

Conventions and model assumptions applied for the derivation of the Stokes coefficients describing the time variations of the external gravity field of the Earth out of globally gridded mass distribution time-series are outlined in Chapter 2. Subsequently, we discuss for individual subsystems atmosphere (AnoIB, Chapter 3), atmosphere including the modified IB-correction (A, Chapter 4), oceans (O, Chapter 5), terrestrial hydrosphere (H, Chapter 6), cryosphere (I, Chapter 7) and the solid Earth (S, Chapter 8) the most important variability pattern, and offer some validation results against observational data. Similar analyses are also presented for the combined model of atmosphere + oceans + terrestrial hydrosphere + cryosphere + solid Earth (AOHIS) in Chapter 9. Sub-diurnal variability at periods shorter than 24 hours is only present in the atmospheric and oceanic component of AOHIS: it will be discussed in Chapter 10 with particular emphasis on atmospheric tides and their oceanic response. Finally, the effects of a doubled temporal and spatial resolution based on high-resoultion data for the single year 2006 are discussed in Chapter 11.

Chapter 2

Technicalities and Conventions

2.1 Spherical Harmonic Analysis

For the analysis of the spherical harmonic coefficients, all mass variation fields of the different models are expressed in surface density variations $\Delta\sigma$. This defines a continuous function $f(\theta, \phi)$ on the sphere which is subsequently expanded into fully normalized spherical harmonic coefficients with Condon-Shortley phase:

$$f_{l,m} = \int_{\sigma} f(\theta, \phi)\, Y^*(\theta, \phi)\, d\sigma \tag{2.1}$$

where (θ, ϕ) are colatitude and longitude and $Y^*(\theta, \phi)$ the conjugate complex surface spherical harmonics of degree l and order m:

$$Y_{l,m}(\theta, \phi) = (-1)^m \sqrt{\frac{2\,l+1}{4\,\pi}\frac{(l-m)!}{(l+m)!}}\, P_{l,m}(\cos\theta)\, e^{im\phi} \tag{2.2}$$

In order to perform the spherical harmonic analysis of the surface mass variations we apply the method proposed by Wang *et al.* (2006). The analysis procedure is based on the assumption that the data are discretized onto grids (i.e. equally spaced or Gaussian grids) and consist of non-smooth data with discontinuous slopes. This can occour in regions of mountain ridges or edges of ocean basins.

The data have to be given in a defined domain of $\theta_a \le \theta \le \theta_b$ and $\phi_a \le \phi \le \phi_b$ and the grid is equally spaced in longitude and latitude direction with the sampling intervals $\Delta\theta$ and $\Delta\phi$. The grid cells are defined by the node rows from 0 at $\theta = \theta_a$ to $i_{\max}$ at $\theta = \theta_b$ and the node columns from 0 at $\phi = \phi_a$ to $j_{\max}$ at $\phi = \phi_b$. Equation (2.1) can be rewritten as:

$$f_{l,m} = \sum_{i=1}^{i_{\max}} \sum_{j=1}^{j_{\max}} \int_{\sigma_{ij}} f(\theta, \phi)\, Y^*_{l,m}(\theta, \phi)\, d\sigma \tag{2.3}$$

The values of $f(\theta, \phi)$ for a specific grid cell can be approximated by a bilinear function:

$$f(\theta, \phi) = f(x, \phi) = A_{ij}\, x + B_{ij}\, \phi + C_{ij}\, x\, \phi + D_{ij} \tag{2.4}$$

with the notation $x = \cos\theta$. The interpolation coefficients (A_{ij}, B_{ij}, C_{ij} and D_{ij}) are determined with function values of the four node points of the grid cell. Therefore, a set of linear algebraic equations has to be solved. For the explicit integration coefficients see Wang *et al.* (2006, Eq. 13).

These integration coeffcients were included in Eq. (2.3) to obtain the equation for the analysis of the spherical harmonic coefficients:

$$f_{l,m} = (-1)^{m+1}\sqrt{\frac{2\,l+1}{4\,\pi}}\sum_{i=1}^{i_{\max}}\left[\int_{x_{i-1}}^{x_i} x\sqrt{\frac{(l-m)!}{(l+m)!}}\,P_{lm}(x)\,dx\right]\sum_{j=1}^{j_{\max}}\left\{\int_{\phi_{j-1}}^{\phi_j}(A_{ij}+C_{ij}\,\phi)\,e^{-im\phi}\,d\phi\right\}$$
$$+\,(-1)^{m+1}\sqrt{\frac{2\,l+1}{4\,\pi}}\sum_{i=1}^{i_{\max}}\left[\int_{x_{i-1}}^{x_i}\sqrt{\frac{(l-m)!}{(l+m)!}}\,P_{lm}(x)\,dx\right]\sum_{j=1}^{j_{\max}}\left\{\int_{\phi_{j-1}}^{\phi_j}(D_{ij}+B_{ij}\,\phi)\,e^{-im\phi}\,d\phi\right\} \tag{2.5}$$

The integration over the longitude in the curly braces is solved analytically using the Fast Fourier Transform. The integration over the latitude in the square braces is solved by using recursion relations for the Legendre Polynomials. The recursion relations are stable up to degree and order 2200 for double precision calculations. A detailed description of the computation is given in Wang *et al.* (2006) in Eq. (15)–(16) and (19)–(21).

The estimated surface spherical harmonic coefficients have to be transferred into geodetically normalized surface spherical harmonics by the relation:

$$\begin{aligned} c_{l0} &= \frac{1}{\sqrt{4\,\pi}}\,f_{l,0} && (m=0)\\ c_{lm} &= \frac{(-1)^m}{\sqrt{2\,\pi}}\,\mathrm{Re}(f_{l,m}) && (m>0)\\ s_{lm} &= \frac{(-1)^{m+1}}{\sqrt{2\,\pi}}\,\mathrm{Im}(f_{l,m}) && (m>0) \end{aligned} \tag{2.6}$$

In a last step, the potential coefficients are obtained out of the mass coefficients following Dong *et al.* (1996):

$$\begin{Bmatrix} C_{lm} \\ S_{lm} \end{Bmatrix} = 4\,\pi\,\frac{a^2}{M_E}\left(\frac{1+k_l^{'}}{2\,l+1}\right)\begin{Bmatrix} c_{lm} \\ s_{lm} \end{Bmatrix} \tag{2.7}$$

where a is the Earth radius and $k_l^{'}$ the elastic Love Number (for further details see section 2.2). The total mass of the Earth M_E can be expressed with G/GM were the standard gravitational constant GM has been chosen identical to Gruber *et al.* (2011).

2.2 Earth Model and Reference Frame

In addition to the redistribution of surface masses, the elastic deformations of the solid Earth under the variable mass load are taken into account in Eq. (2.7) via the Load Love number $k_l^{'}$. The Earth System Model will also include mass redistribtions in the earth's interior, like earthquakes and glacial isostatic adjustments, so horizontal and vertical displacements will also lead to changes in the potential of the solid Earth. Therefore, the mass components of the subsystem will be referenced to the Center of surface Figure (CF) frame. For Eq. (2.7) it means, that changes in the degree 1 Load Love number $k_n^{'}$ have to be included.

We used the Load Love numbers computed by Pascal Gegout (pers. commun.) given in the Center of Mass of the Earth System (CM) frame. Transfering Load Love numbers from one frame to another implies a translation of the frame-origin. Therefore, solely the degree-1 terms will be affected by this. The translation of the k_1 Load Love number from the CM to the CF follows Blewitt (2003):

$$\left[1+k_1^{'}\right]_{CF} = \left[-\frac{1}{3}\,h_1^{'} - \frac{2}{3}\,l_1^{'}\right]_{CM} \tag{2.8}$$

The first ten Load Love numbers are given in Table 2.1.

Table 2.1: Elastic Load Love Numbers k_l computed by P. Gegout for the PREM Earth model

l	k_l
0	+0.000
1	+0.026
2	-0.305
3	-0.196
4	-0.134
5	-0.105
6	-0.090
7	-0.082
8	-0.077
9	-0.072
10	-0.069

2.3 Available Datasets and Format Description

All data-sets of the updated ESM are provided in ascii files; where format conventions applied are identical to the original dataset of Gruber *et al.* (2011). The updated ESM is available at DOI:10.5880/GFZ.1.3.2014.001. The files are organized into three different directories:

mtmshc

This directory contains spherical harmonic coefficients for the individual components of the updated ESM, namely the IB-corrected atmosphere (A), ocean (O), the terrestrially stored water (H), land ice (I), and solid Earth effects (S). In addition, the sum of all five components is given as AOHIS. All data-sets have a spectral resolution of d/o = 180, and a temporal resolution of 6 hours. The data is available for the years 1995 until 2006, files are grouped for each year in tar archives.

mtm3h

The updated ESM additionally provides high-resolution data-sets with 3 hourly sampling and a spectral resolution of d/o = 360 for the year 2006. Individual components (A, O, H, I, S) are available together with the sum of all five components AOHIS. The data is grouped into monthly tar archives.

Moreover, a second high-resolution data-set for the atmosphere is available for 2006 where mass variability over Europe is replaced by model predictions of the regional atmospheric model COSMO-EU. The component is abbreviated as 'Ac'. Consequently, a second sum of the five components that includes COSMO-EU is provided under the label 'AcOHIS'.

mtmnIB

In addition to the IB-corrected atmospheric component, there is an additional atmospheric data-set without the application of the IB-correction over the oceans (AnoIB). The component has a spectral resolution of d/o = 180, a temporal sampling of 6 hours, and covers the years 1995 until 2006. Individual files are grouped into yearly tar archives. Note that there is no sum that includes AnoIB, since the sum of A and O is identical to AnoIB and OnoIB per definition of the IB-correction.

Chapter 3

Atmospheric Mass Variability

3.1 ERA-Interim Surface Pressure Anomalies

The latest re-analysis from ECMWF, ERA-Interim (Dee *et al.*, 2011), is currently available from 1979 - 2013 and represents a synthesis of all available information on the evolution of the state of the atmosphere over the last decades. Although the physical model, the numerical scheme, and the data assimilation framework of ERA-Interim were not changed during the re-analysis period, systematic biases related to changes in the observation network or related to volcano-induced atmospheric disturbances cannot be excluded. Compared to other available atmospheric re-analysis data sets, however, ERA-Interim performs favourably well, in particular with respect to the representation of the atmospheric branch of the global water cycle (Lorenz & Kunstmann, 2012). We use 6 hourly surface pressure data sets discretized horizontally at 0.5° equiangular grids that were downloaded directly from the ECMWF archives.

From the full 12 year period considered for the updated Earth System Model, we estimate and remove the mean signal of the semi-diurnal atmospheric tide $S_2(p)$ from the ERA-Interim surface pressure grids, since variability at this period is partly aliased in a 6-hourly sampled data-set. The remaining signal content at sub-daily periods including the diurnal tide $S_1(p)$ will be discussed in Chapter 10.

3.2 Characteristics of Component AnoIB

The spherical harmonics of component AnoIB are synthesized on a global grid, and the time-series at each grid point is analysed. We identify linear trends of up to 0.4 hPa in particular in the North Pacific, where the Pacific Decadal Oscillation dominates the decadal pressure variability (Fig. 3.1). Weaker trend pattern are also identified around Island and the Azores in the North Atlantic, where the corresponding pressure systems that are associated with the North Atlantic Oscillation are positioned. Similar signals are also identified at the corresponding latitudes of the Southern Hemisphere. Over the continents, trends are substantially smaller, but show nevertheless pattern that are coherent over large areas, as for example, in the Himalaya, or over Greenland.

Variability contained in de-trended time-series of daily means reaches rms values of up to 15 hPa in particular over oceanic regions in middle latitudes (Fig. 3.2). Variability systematically decreases towards the equator down to about 2 hPa. Note that sub-daily variability including tides do not contribute to the rms values shown here, since only daily means have been considered. Sub-daily variations will be treated separately in Chapter 10.

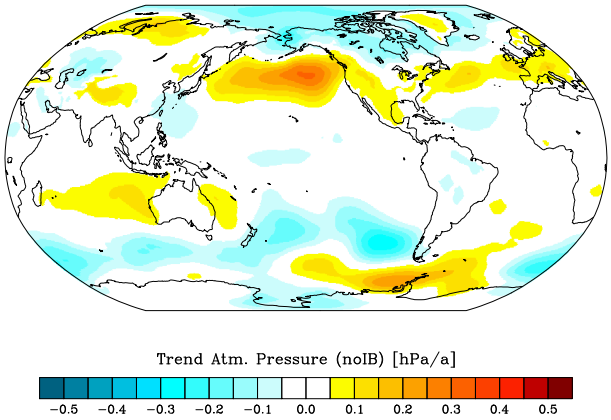

Figure 3.1: Local secular trends (1995-2006) at 0.5° spatial resolution obtained from the re-synthesized coefficients of the AnoIB component from the updated ESM.

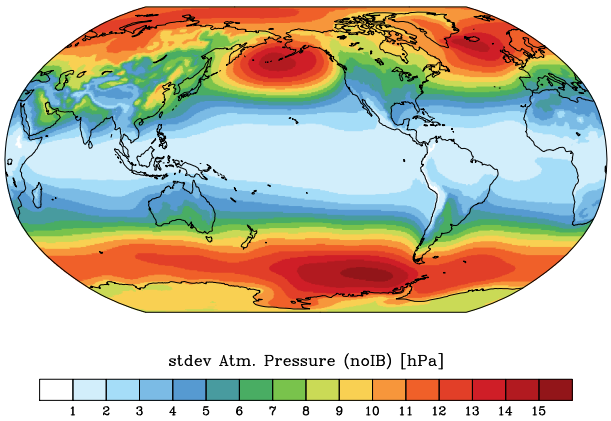

Figure 3.2: Standard deviation of atmospheric surface pressure anomaly (non-IB) (1995-2006) at 0.5° spatial resolution obtained from the re-synthesized and locally detrended coefficients of the AnoIB component from the updated ESM.

By separating the variability into periods longer (Fig. 3.3) and shorter (Fig. 3.4) than 30 days by applying a 3rd order Butterworth filter to the time-series of each grid point, we note that the high-frequency variability dominates over the low-frequency changes in areas as Northern Russia or Canada, and also over many oceanic regions. This high-frequency variability is a potential source of aliasing errors within the final gravity retrieval of a simulation, and it is important to have it included in the updated ESM to arrive at realistic simulation scenarios.

3.3 Validation against ITG3D

In order to demonstrate the realism of the atmospheric component AnoIB of the updated ESM, we perform comparisons with a more complete atmospheric de-aliasing product prepared within the context of the GRACE mission. The product ITG3D (Forootan *et al.*, 2013) is based on ERA-Interim atmospheric data, but performs a numerical integration over the atmospheric masses at different altitudes instead of only considering the surface pressure.

Comparisons of low-degree spherical harmonic coefficients (Fig. 3.5) of the updated ESM with ITG3D for the year 2006 reveal very close correspondence at all important frequencies. We additionally compared variability of the re-synthesized models on the grid and find very similar patterns

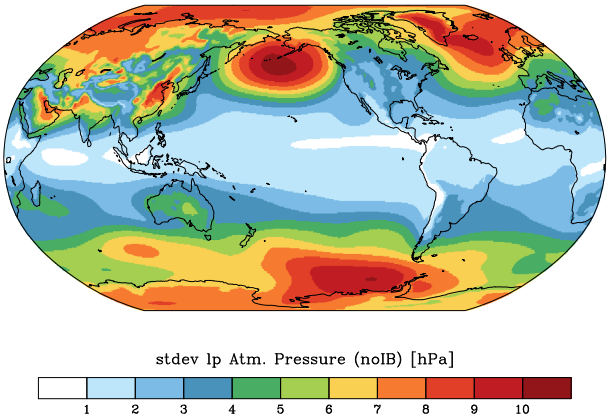

Figure 3.3: Standard deviation of atmospheric surface pressure anomaly (non-IB) (1995-2006) at 0.5° spatial resolution obtained from the re-synthesized, locally detrended and low-pass filtered (30 day cut-off) coefficients of the AnoIB component from the updated ESM.

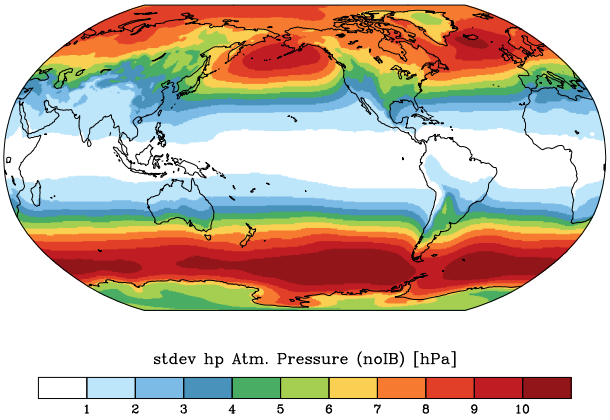

Figure 3.4: Standard deviation of atmospheric surface pressure anomaly (non-IB) (1995-2006) at 0.5° spatial resolution obtained from the re-synthesized, locally detrended and high-pass filtered (30 day cut-off) coefficients of the AnoIB component from the updated ESM.

(Fig. 3.6).

We also perform a Principal Component Analysis (PCA; Preisendorfer, 1988) to both ITG3D and the AnoIB component of the updated ESA ESM. The method decomposes a time-series into orthogonal modes (i.e., spatial and temporal uncorrelated components) that represent the dominant features of the atmospheric mass variability in the year 2006. The empirical orthogonal functions represent the spatial pattern, whereas the time variability is represented by the principal components associated with the EOFs.

PCA analyses are performed independently for ITG3D and the component AnoIB, but nevertheless reveal very similar leading EOF patterns for both data-sets (Fig. 3.7). The corresponding principal components are nearly identical as well (Fig. 3.8), so that we conclude that the dominant mass variations in the atmosphere are indeed very well reflected by the surface pressure so that 3D information does not need necessarily to be included into a source model suitable for gravity satellite simulation studies.

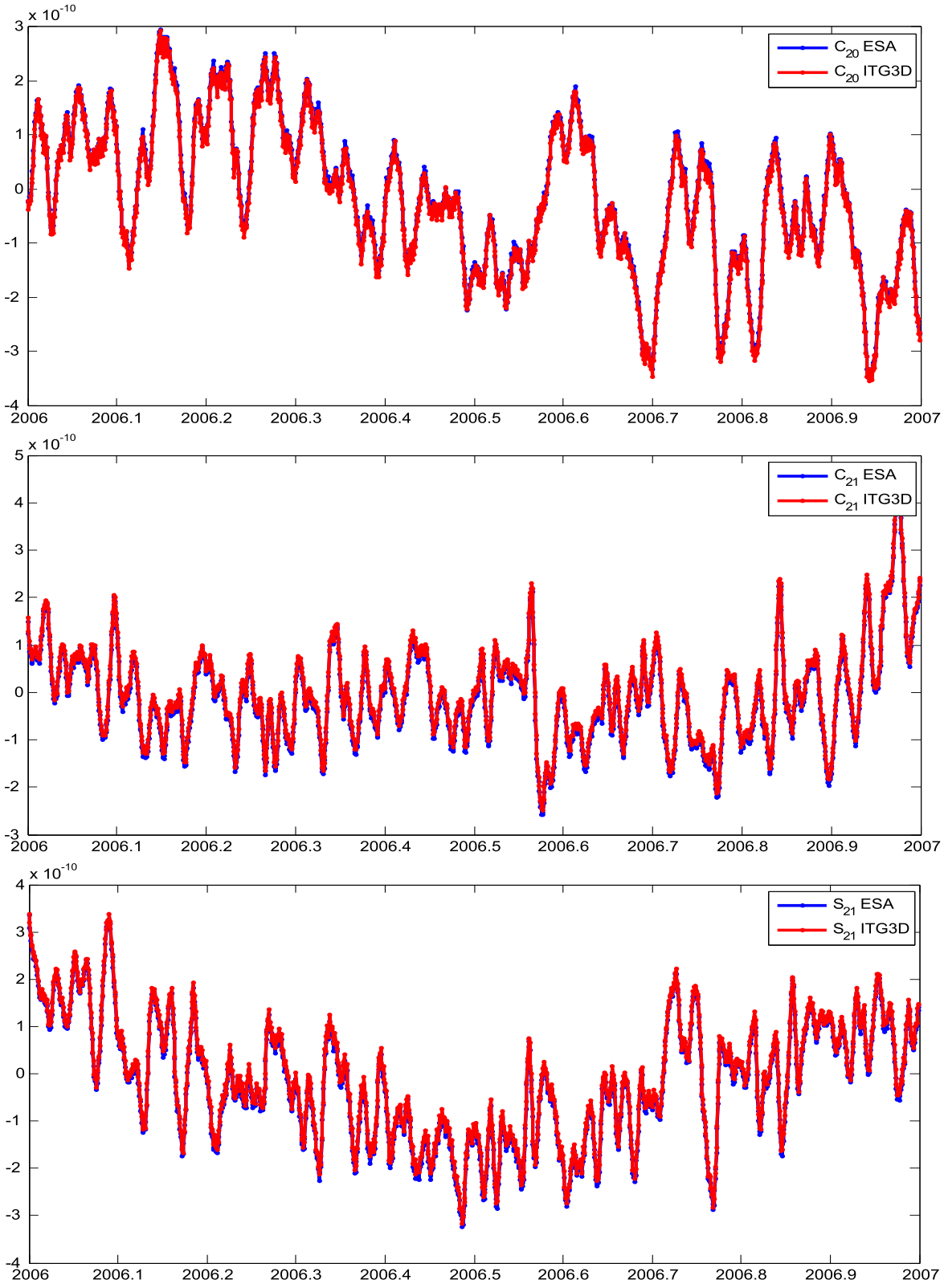

Figure 3.5: Time series (1995-2006) of degree two spherical harmonic coefficients of atmospheric surface pressure anomaly (non-IB) from the updated ESM AnoIB component (blue) and ITG3D (red).

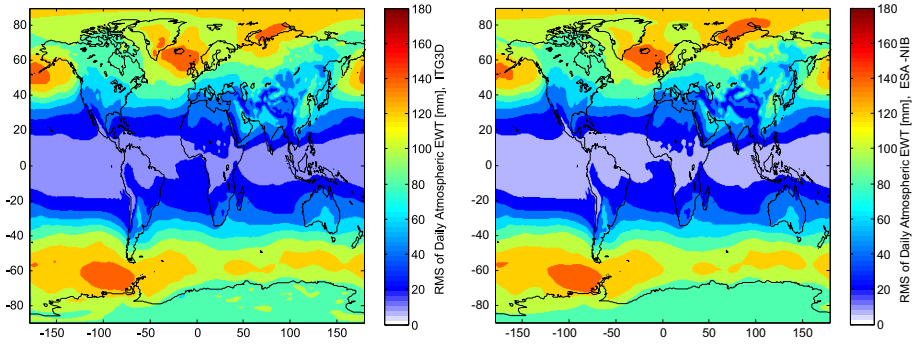

Figure 3.6: RMS of atmospheric surface pressure (non-IB) for the year 2006 of ITG3D (left) and updated ESM AnoIB component (right).

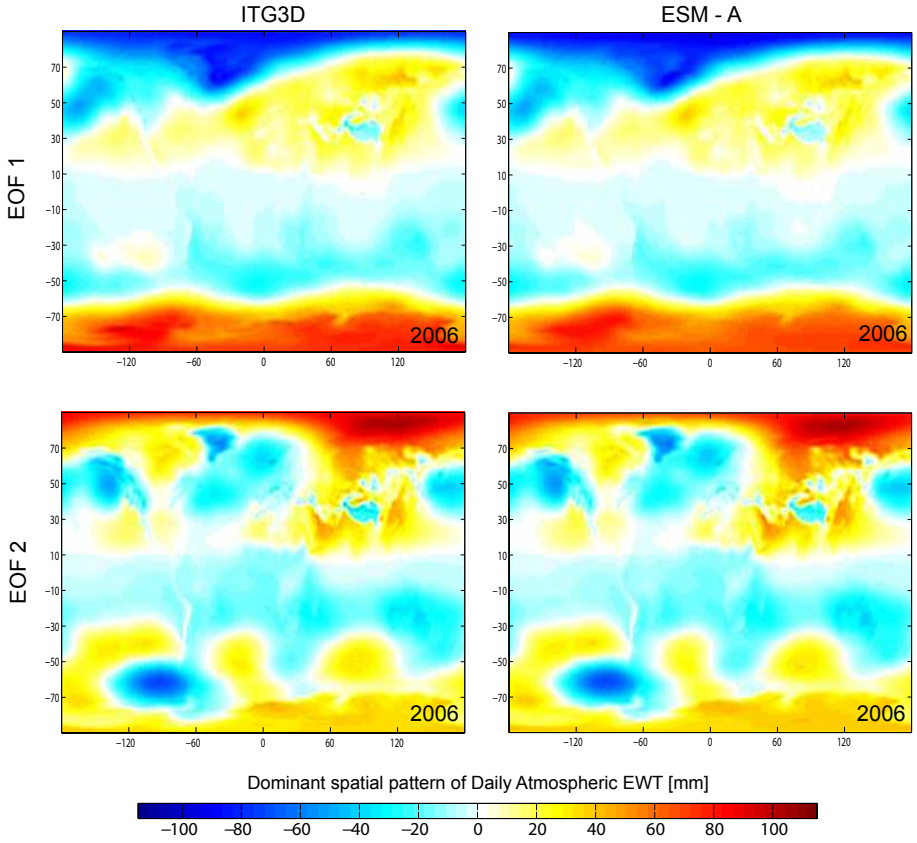

Figure 3.7: Spatial pattern of the first and second dominant Empirical Orthogonal Function (EOF1, EOF2) for atmospheric surface pressure anomaly (non-IB) for the year 2006 of ITG3D (left) and updated ESM AnoIB component (right).

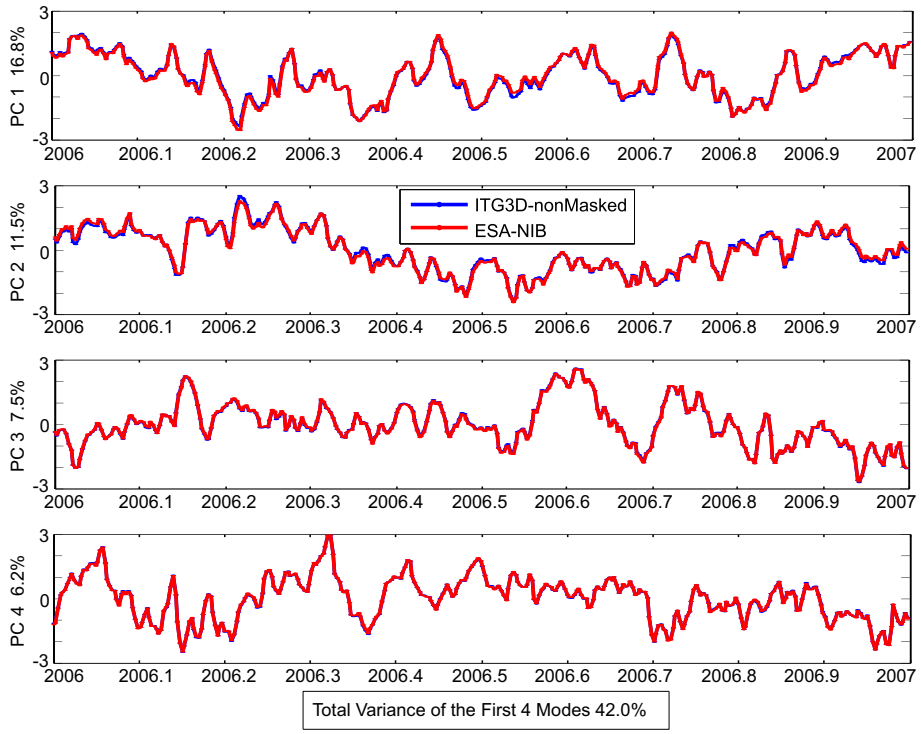

Figure 3.8: Temporal variability of the first four dominant modes (PC 1 - PC 4) for atmospheric surface pressure anomaly (non-IB) for the year 2006 of ITG3D (blue) and updated ESM AnoIB component (red).

Chapter 4

Inverse-Barometrically Corrected Atmospheric Mass Variability

4.1 Modified IB-Correction: Consequences for the Atmospheric Component

Ocean-bottom pressure is commonly regarded as the summarized effect of the hydrostatic pressure of both the atmospheric and oceanic masses situated along the plumb line above a certain position of the ocean sea-floor. For the representation of global bottom pressure in model data-sets, those masses are traditionally separated into an atmospheric and an oceanic contribution, a convention that is both applied in the current GRACE AOD1B product (Flechtner & Dobslaw, 2013), and also in the original ESA ESM (Gruber *et al.*, 2011).

The local sea-surface, however, reacts rapidly to changes in atmospheric surface pressure. As evidenced from the analysis of global sea-level variations observed with satellite altimetry, the ocean is adjusting almost perfectly to surface pressure changes on periods of a few days and longer (Wunsch & Stammer, 1997). Thus, atmospheric and oceanic contributions to ocean-bottom pressure are highly correlated, and largely cancel each other when summarized.

To remove the correlation between the atmospheric and oceanic components of ocean-bottom pressure, we apply the so-called modified IB-correction to the oceanic component, which requires to add the difference between the actual atmospheric surface pressure and the mean atmospheric surface pressure averaged over all oceanic regions to the oceanic pressure component at each time instance. To keep the actual bottom pressure unchanged by this modification, the same term is consequently subtracted from the atmospheric surface pressure at each grid point, which essentially leads to a replacement of the acual atmospheric surface pressure with the mean atmospheric surface pressure averaged over all oceanic regions in the atmospheric component A of the updated ESM.

We would like to emphazise once more that bottom pressure at the sea-floor is not affected by this modified IB-correction whatsoever. But applying the modified IB-correction largely de-correlates the atmospheric and oceanic components, and therefore allows to treat them as independent contributors to the time-variable gravity field in subsequent sensitivity analyses. Moreover, the dynamical interpretation of the ocean component is eased substantially, since it now closely resembles the bottom pressure instead of rather reflecting the sea-level adjustment to atmospheric surface pressure changes.

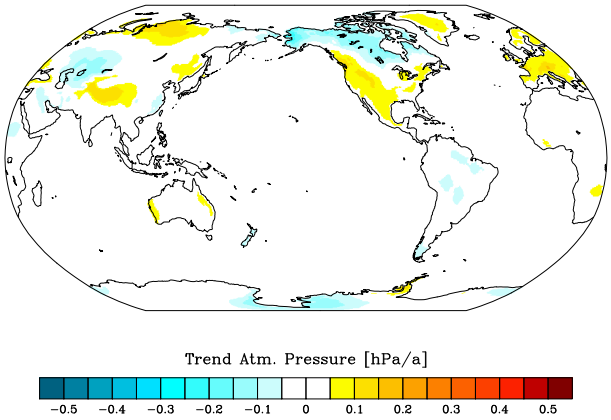

Figure 4.1: Local secular trends (1995-2006) at 0.5° spatial resolution obtained from the re-synthesized coefficients of the A component from the updated ESM.

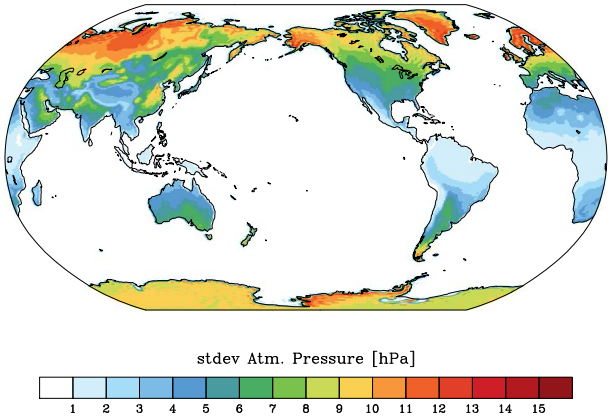

Figure 4.2: Standard deviation of atmospheric surface pressure anomaly (IB-corrected) (1995-2006) at 0.5° spatial resolution obtained from the re-synthesized and locally detrended coefficients of the A component from the updated ESM.

4.2 Characteristics of Component A

The linear trends of the IB-corrected component A of the updated ESM over the continents (Fig. 4.1) are identical to the AnoIB component discussed in the previous chapter. Over the oceans, trends are no longer visible since drifts in the mean atmospheric surface pressure averaged over all oceanic regions that replaces the actual surface pressure under the IB-correction are now very small. In addition, also the variability (Fig. 4.2) is not changed over the continents but is now well below 1 hPa in oceanic regions, thereby indicating that the static contribution of the atmosphere to ocean-bottom pressure is quite small, but nevertheless non-negligible.

4.3 Validation against ITG3D

We also repeat the comparisons with ITG3D presented in the previous chapter. Since ITG3D does not apply the IB-correction, we re-synthesize both products onto the same grid and apply the AOD1B landmask as it is convention for all components of the updated ESM. Variability over the year 2006 (Fig. 4.3), as well as EOFs (Fig. 4.4) and PCs (Fig. 4.5) from a repeated PCA analysis support our conclusion, that also the IB-corrected component A of the updated ESM is over the

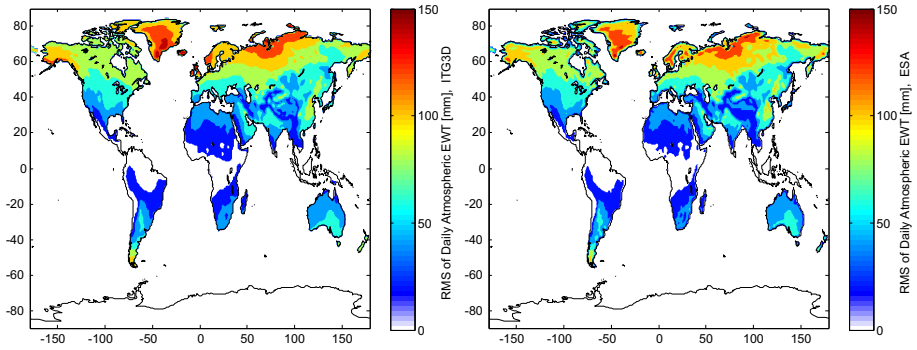

Figure 4.3: RMS of atmospheric surface pressure (IB-corrected) for the year 2006 of ITG3D (left) and updated ESM A component (right).

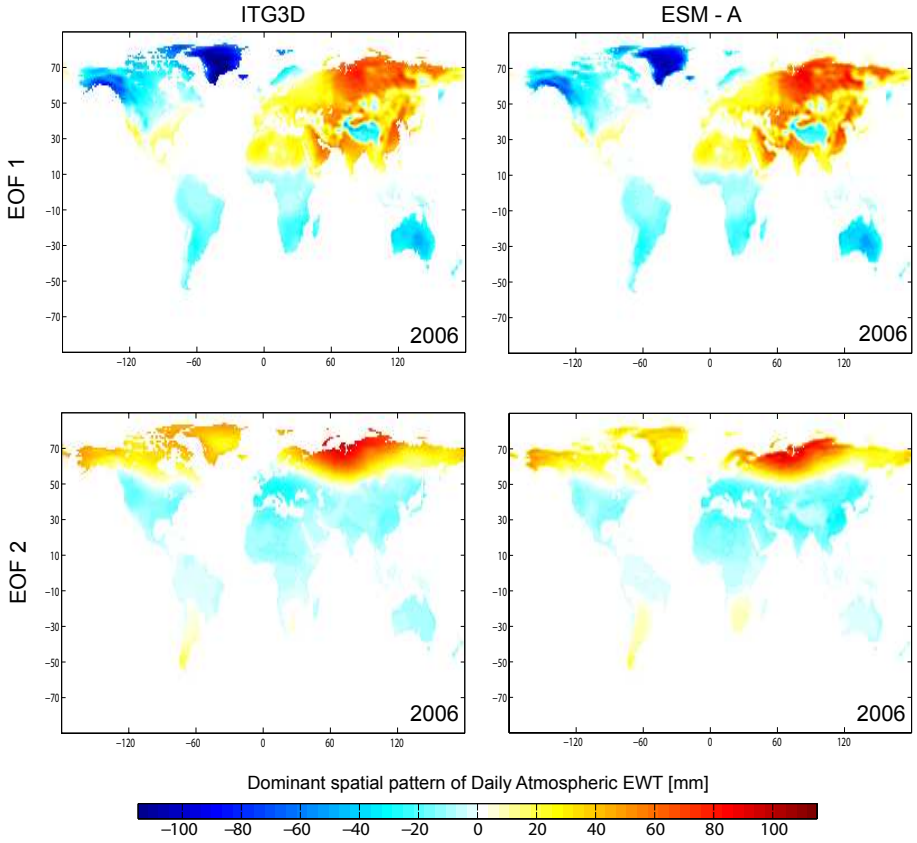

Figure 4.4: Spatial pattern of the first and second dominant Empirical Orthogonal Function (EOF1, EOF2) for atmospheric surface pressure anomaly (IB-corrected) for the year 2006 of ITG3D (left) and updated ESM A component (right).

continents very close to independently calculated more complete atmospheric de-aliasing products.

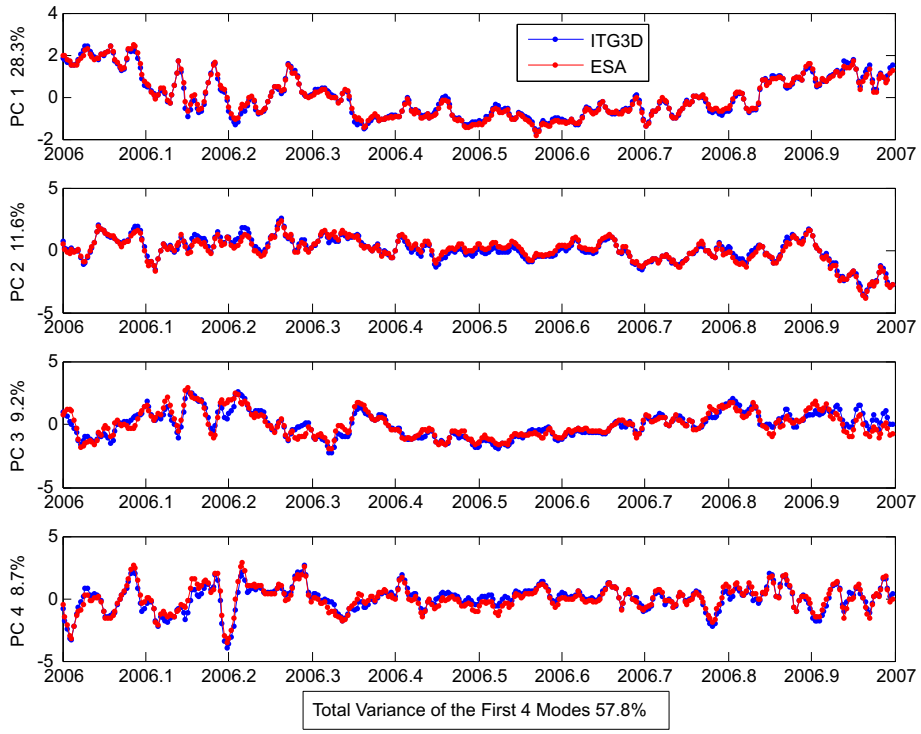

Figure 4.5: Temporal variability of the first four dominant modes (PC 1 - PC 4) for atmospheric surface pressure anomaly (IB-corrected) for the year 2006 of ITG3D (blue) and updated ESM A component (red).

Chapter 5

Ocean Bottom Pressure Variability

5.1 Bottom Pressure Anomalies from OMCT and STORM

The Ocean Model for Circulation and Tides (OMCT; Thomas *et al.*, 2001) is used since the year 2006 as a standard background model to remove non-tidal ocean mass variability from GRACE observations. For the latest reprocessing RL05, a new OMCT version discretized at 1.0° has been incorporated (Dobslaw *et al.*, 2013). Compared to both satellite altimetry and deep-sea pressure gauges, the model performs favourably well in explaining the bottom pressure variability at periods below 30 days (see www.gfz-potsdam.de/aod1b for details). Here, we use OMCT simulations in an identical setting as applied for GRACE AOD1B RL05, but forced with atmospheric data from ERA Interim in order to avoid any inconsistencies related to changes in the ECMWF operational analysis model. Bottom pressure grids are available every 6 hours for the period 1995 - 2006.

We start with ocean-bottom pressure estimates from the numerical simulations that comprise pressure contributions from both the air column above sea-level, and the water column below it. We subtract the area-averaged atmospheric surface pressure, since this is already contained in the A component of the updated ESM. We further estimate and remove any tiny variations in total ocean mass that are present in the numerical model data due to the application of the Boussinesq approximation in OMCT. Further, the oceanic response to the atmospheric tide $S_2(p)$ at the semi-diurnal frequency is estimated and removed as it has been equally done for the atmospheric part. We also remove the local secular trends over the 12 years period considered here, since those trends are believed to be less reliable in OMCT simulations (Dobslaw *et al.*, 2013). Finally, a time-mean bottom pressure field for the full period between 1995 and 2006 is calculated and removed in order to arrive at bottom pressure anomalies as input for the spherical harmonics analysis step.

While OMCT provides state-of-the-art estimates of high-frequency ocean bottom pressure variability, its limited spatial resolution does not provide information on meso-scale variability. A recent experiment from the MPIOM ocean model - which shares with OMCT its heritage from the Hamburg Ocean Primitive Equation model HOPE (Drijfhout *et al.*, 1996; Wolff *et al.*, 1997) - has been integrated over four decades with a configuration at very high resolution of 0.1° on a tripolar curvilinear grid (Storch *et al.*, 2012). Bottom pressure from this experiment is only available at daily averages and thus lacks a substantial fraction of the high-frequency variability, but it contains dominant small-scale ocean bottom pressure variability in regions of distinct meso-scale upper ocean variability and steep gradients in bathymetry. Since those signals are found to have auto-correlation length scales of several days, they might be principally observable by a third generation gravity mission, thus allowing a contribution of satellite gravimetry to understand the meso-scale upper ocean variability. Since meso-scale variability is uniquely represented by the Stokes coefficients of high degree and order not resolved by OMCT, we combine both datasets in the spectral domain,

where OMCT provides the lower spherical harmonic degrees up to d/o 60, and MPIOM contributes the small-scale information at higher degrees and orders.

As for OMCT, variations in total ocean mass from MPIOM are estimated and removed. Further, local secular trends and mean values calculated for the period 1995 - 2006 are subtracted. The remaining residuals are linearly interpolated to 6 hourly time-steps concurrent with ERA Interim and OMCT for subsequent combination.

5.2 Eustatic Sea-Level Variability

The updated ESM requires specifically to preserve the sum of all masses stored on the continents, in the atmosphere, and the oceans. Both OMCT and MPIOM simulations described before, however, do not include eustatic variations in global sea-level due to exchange of water masses with the continents. But numerical simulations with general ocean circulation models demonstrate that even very large and localized melt water pulses spread out equally over the global ocean within a few days only (Dobslaw & Thomas, 2007; Lorbacher *et al.*, 2012), leading to a globally homogeneous response of the ocean-bottom pressure field to freshwater inflow that changes the total ocean mass. This property was utilized for example to derive changes in the total ocean mass from observations of a single bottom pressure mooring the central Pacific alone (Hughes *et al.*, 2012). Thus, as long as loading and self-attraction feedbacks on the sea-level dynamics are omitted, the barotropic response of the ocean to changes in total ocean mass can be calculated separately from the integration of the ocean general circulation.

Total masses contained in the atmospheric part (the A component, see Chapter 4), the terrestrial part (the H component, see Chapter 6), and the cryospheric part (the I component, see Chapter 7) of the updated ESM are accumulated at each individual time-step. Since all components only contain mass anomalies that fluctuate around zero, the additive inverse of the accumulated mass determines the global eustatic sea-level anomaly. The globally homogeneous surface mass anomaly $\Delta\sigma(\theta,\phi)$ that represents the eustatic sea-level variation therefore depends only on the degree-0 coefficients of the A, H, and I components of ESA ESM:

$$\Delta\sigma(\theta,\phi) = -\frac{\Omega}{\Omega_{Oc}}\tilde{P}_{00}(\cos\theta)\{\Delta C^{A}_{00} + \Delta C^{H}_{00} + \Delta C^{I}_{00}\}, \tag{5.1}$$

which can be finally analyzed into sherical harmonic coefficients up to d/o = 180 by employing the land-ocean mask $\vartheta(\theta,\phi)$

$$\Delta C^{esl}_{lm} = \frac{1}{4\pi}\int d\Omega\ \tilde{P}_{lm}(\cos\theta)\cos m\phi\ \vartheta(\theta,\phi)\ \Delta\sigma(\theta,\phi). \tag{5.2}$$

The ocean part (the O component) of the updated ESM thus is a linear combination of large-scale ocean-bottom pressure anomalies from OMCT (up to d/o 60), of small-scale ocean-bottom pressure anomalies from MPIOM (d/o 61 to 180), and globally homogeneous sea-level changes derived from the accumulated mass anomalies contained in the A, H, and I components of the updated ESM.

5.3 Characteristics of Component O

The pattern of the linear trend in component O of the updated ESM is dominated by 0.98 mm a^{-1} global eustatic sea-level rise (Fig. 5.1). Superimposed to this global signal, we note wind-driven effects in several regions at moderate to high latitudes that amount to 0.3 hPa a^{-1} regionally.

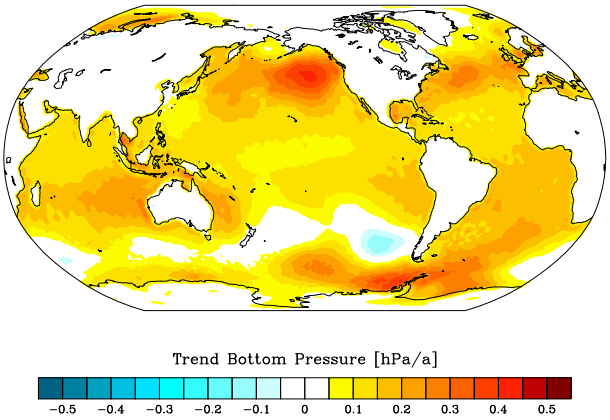

Figure 5.1: Local secular trends (1995-2006) at 0.5° spatial resolution obtained from the re-synthesized coefficients of the O component from the updated ESM.

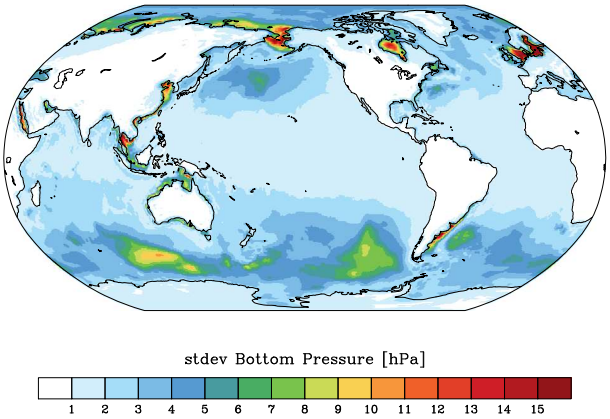

Figure 5.2: Standard deviation of ocean-bottom pressure anomaly (1995-2006) at 0.5° spatial resolution obtained from the re-synthesized and locally detrended coefficients of the O component from the updated ESM.

Variabilitity contained in de-trended time-series of daily means reaches rms values of up to 15 hPa in particular in shallow shelf regions as Bering Strait or in the North Sea (Fig. 5.2). Variability systematically decreases towards the equator down to about 2 hPa. Note that sub-daily variability including the oceanic response to atmospheric tides do not contribute to the rms values shown here, since only daily means have been considered. Sub-daily variations will be treated separately in Chapter 10.

By separating the variability into periods longer (Fig. 5.3) and shorter (Fig. 5.4) than 30 days by applying a 3rd order Butterworth filter to the time-series of each grid point, we note that the high-frequency variability dominates over the low-frequency changes in several places in the Southern Ocean. This high-frequency variability is a potential source of aliasing error within the final gravity retrieval of a simulation, and it is important to have it included in the updated ESM to arrive at realistic simulation scenarios.

In addition, we note substantially smaller spatial scales in the low-frequency variability plot (Fig. 5.3), as, for example, in the Argentine Basin in the Western South Atlantic. Here, high eddy kinetic energy causes small-scale bottom pressure variability that is characterised by time-scales of weeks to months, that might be a potential target signal for a future satellite gravity mission, since it has not been reliably observed by GRACE so far.

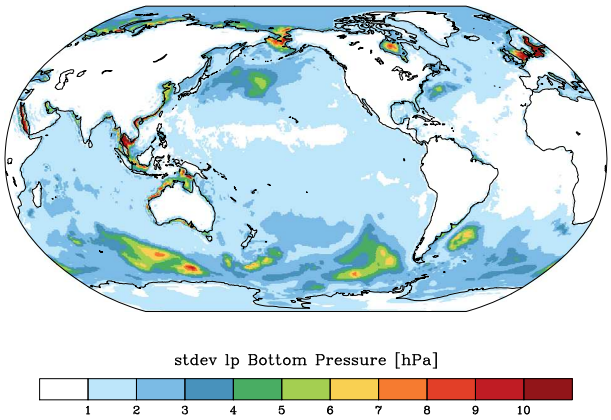

Figure 5.3: Standard deviation of ocean-bottom pressure anomaly (1995-2006) at 0.5° spatial resolution obtained from the re-synthesized, locally detrended and low-pass filtered (30 day cut-off) coefficients of the O component from the updated ESM.

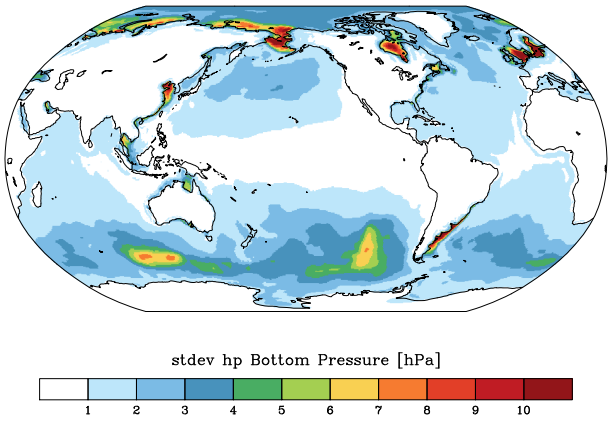

Figure 5.4: Standard deviation of ocean-bottom pressure anomaly (1995-2006) at 0.5° spatial resolution obtained from the re-synthesized, locally detrended and high-pass filtered (30 day cut-off) coefficients of the O component from the updated ESM.

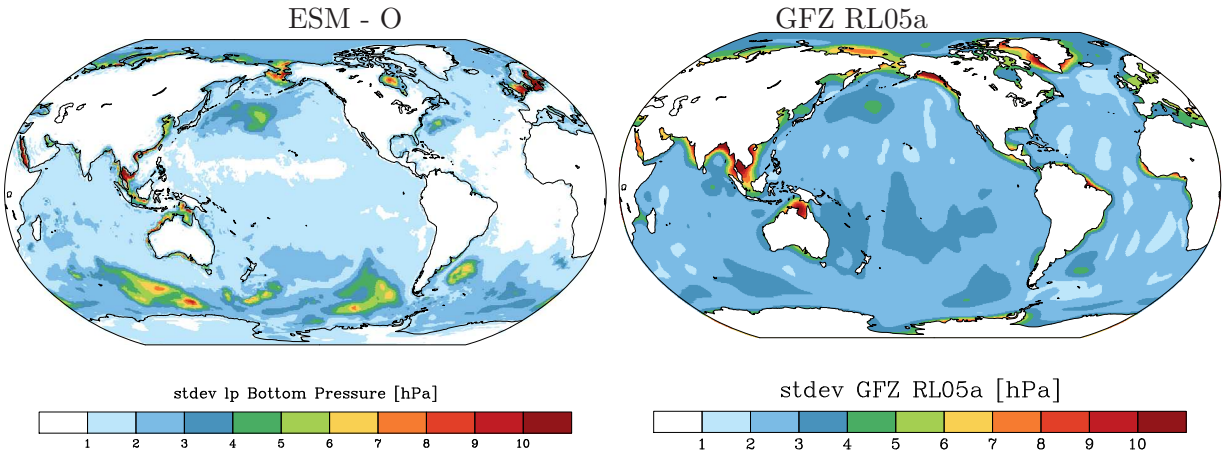

Figure 5.5: Standard deviation (1995-2006) of ocean-bottom pressure anomaly (left) at 0.5° spatial resolution obtained from the re-synthesized coefficients of the O component from the updated ESM, and right, locally detrended and low-pass filtered (30 day cut-off) and GRACE GFZ RL05 (GAC) monthly mass anomaly, DDK2 filtered.

5.4 Validation with GRACE

We employ results from the GRACE mission to evaluate the realism of the O component of the updated ESM. GRACE RL05 gravity fields processed at GFZ Potsdam that are postprocessed with DDK2 (Kusche, 2007) show variability of about 5 hPa in moderate and high latitudes, that corresponds favourably with the regions where the updated ESM has signals at the same frequency band (Fig. 5.5). Note that spatial gradients in the GRACE solution are substantially diminished due to the limited spatial resolution abilities of GRACE and the applied post-processing filter.

For the high-frequency signals at periods below 30 days, we make use of the daily GRACE solutions from University of Bonn (Kurtenbach *et al.*, 2009). The updated ESM does indeed show signals in very similar regions, and also the amplitudes are - apart from localized peaks not resolvable by GRACE - very well comparable (Fig. 5.6). We therefore conclude that the updated ESM does indeed contain realistic bottom pressure variability at both high- and low-frequency bands.

Besides using GRACE as a validation data-set, the OMCT simulations for GRACE AOD1B RL05 have been extensively validated with both in situ ocean bottom pressure observations and high-pass filtered sea-level anomalies from satellite altimetry (Dobslaw *et al.*, 2013). Since OMCT simulations used for the updated ESM do only differ in the atmospheric forcing applied, they provide very similar bottom pressure predictions as in AOD1B RL05. Conclusions drawn in that paper are therefore largely transferable to the O component of the updated ESM.

We also estimate the global eustatic sea-level variability out of the O component of the updated ESM and contrast it to GRACE GFZ RL05 results as obtained by Bergmann-Wolf *et al.* (2014b). Annual amplitudes are with 6.28 mm substantially smaller than 10.16 mm as obtained from GRACE. Phases are, however, with peaks at 278 and 288 days very consistent (Fig. 5.7). For the global mean trends, we find 0.98 mm a^{-1} for updated ESM in contrast to 1.36 mm a^{-1} (Fig. 5.8). Note however, that this discrepancy is largely caused by the different time-periods available: In the updated ESM, almost no sea-level trend is apparent during the first three years, that is followed by a rapid acceleration related to increasing ice-mass loss after the year 2000. Over the common period 2003 - 2006, eustatic sea-level trends from GRACE and the updated ESM have about the same size.

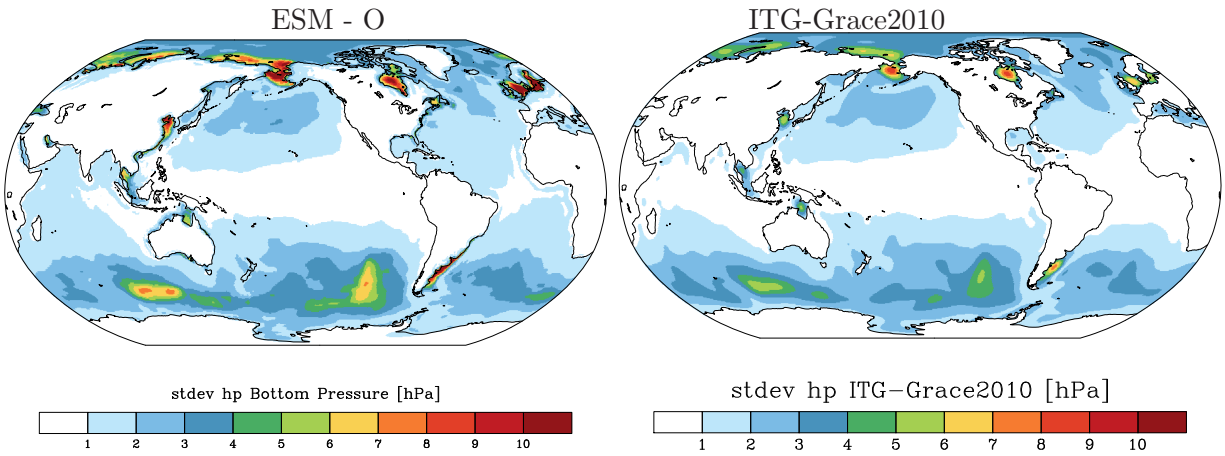

Figure 5.6: Standard deviation (1995-2006) of ocean-bottom pressure anomaly (left) at 0.5° spatial resolution obtained from the re-synthesized coefficients of the O component from the updated ESM, and right, locally detrended and high-pass filtered (30 day cut-off) ITG-Grace2010.

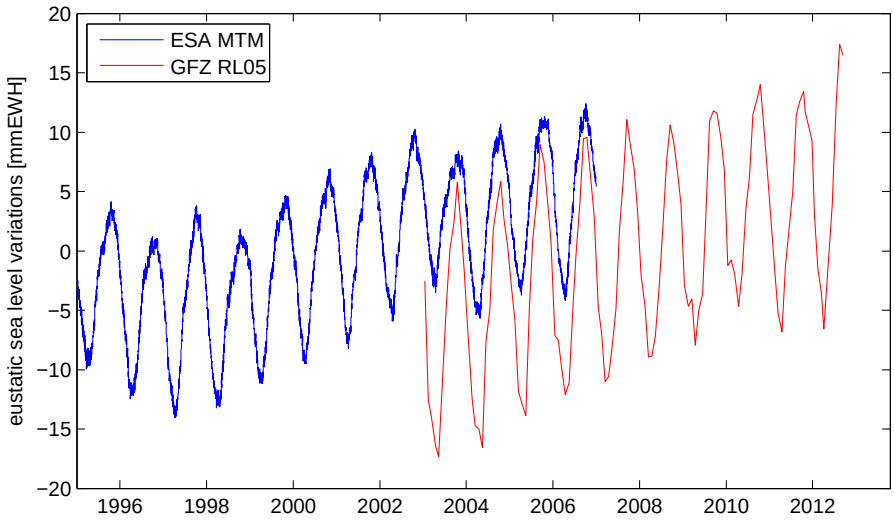

Figure 5.7: Eustatic sea-level variability of updated ESM (1995-2006) in blue and GRACE GFZ RL05 (2003-2012) in red.

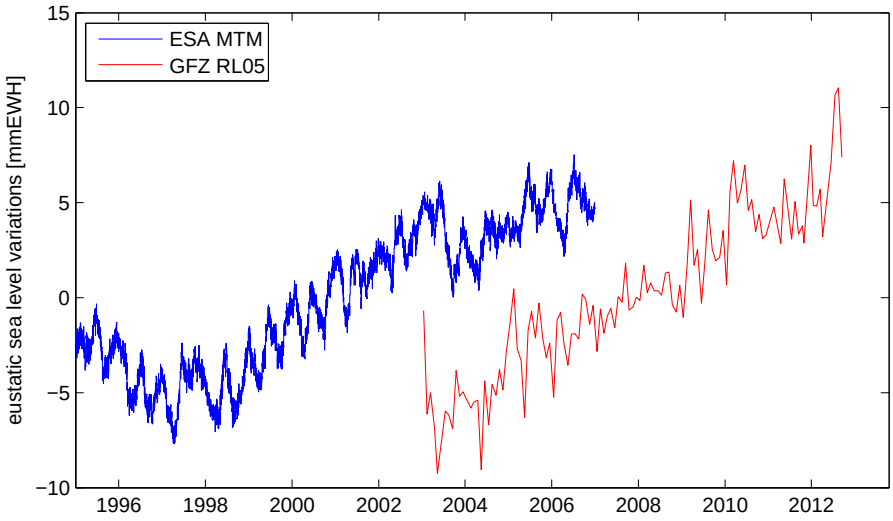

Figure 5.8: Trend in eustatic sea-level variability, seasonal signal removed, of updated ESM(1995-2006) in blue and GRACE GFZ RL05 (2003-2012) in red.

Chapter 6

Terrestrial Water Storage Changes

6.1 Terrestrial Water Variability from LSDM

Forced with atmospheric freshwater and energy fluxes from ERA-Interim, the Land Surface Discharge Model (LSDM; Dill, 2008) simulates vertical and lateral water transport and storage on land surfaces. Physics and parametrisation of LSDM are based on Hagemann & Dümenil (1997), and include the representation of soil moisture, snow storage, and water stored in rivers and lakes (Fig. 6.1). The model is discretized on a 0.5° equiangular grid and provides mass estimates at daily time intervals. LSDM mass anomalies are applied at GFZ Potsdam for a number of geodetic applications, including the calculation of effective angular momentum functions for changes in the Earth's rotation (Dill & Dobslaw, 2010), as well as for the assessment of crustal deformations seen in geodetic station position time-series (Dill & Dobslaw, 2013). Global mass anomalies from LSDM are available for the period 1995 - 2006 at daily time intervals.

LSDM is in particular well suited to study spatial aliasing effects in time-variable gravity field retrievals, since it also includes mass anomalies from surface water bodies as rivers or lakes which are often opposite in phase compared to the mass anomalies related to the surrounding soil moisture

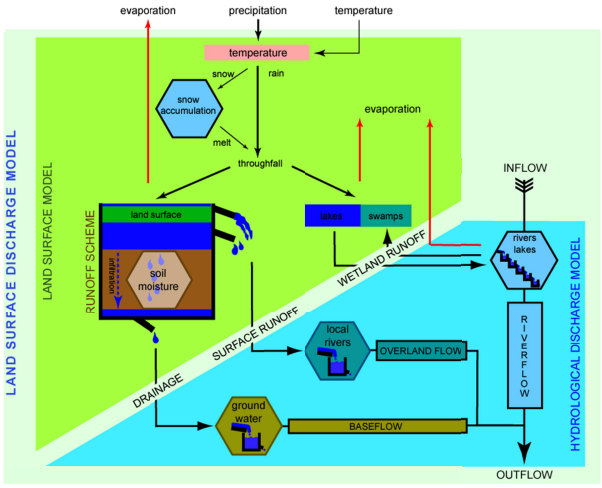

Figure 6.1: Flow chart of the global hydrological Land Surface Discharge Model (LSDM). Vertical water balance is given by the land surface module, forced with atmospheric input of precipitation, evaporation, and temperature. Horizontal water balance is given by the discharge module interacting with the land surface by drainage (baseflow), surface runoff, and wetland runoff. Individual 0.5°x.0.5° gridcell are interacting via the riverflow.

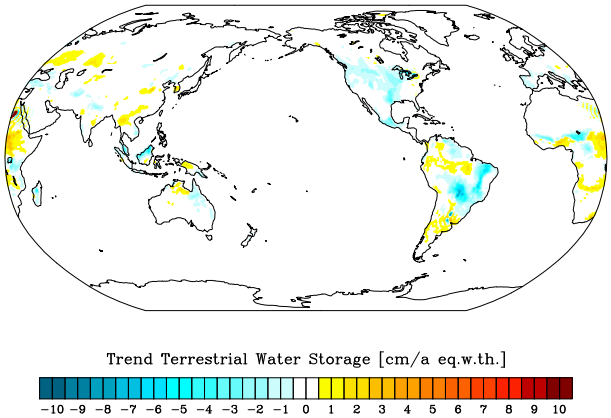

Figure 6.2: Local secular trends (1995-2006) at 0.5° spatial resolution obtained from the re-synthesized coefficients of the H component from the updated ESM.

or snow cover. In addition, LSDM contains an empirical parametrisation for the seasonal water management at Lake Nasser (Egypt), leading to locally concentrated water mass variations there. Note that, in contrast to the original Earth System Model (Gruber *et al.*, 2011), glacier mass losses in Alaska, the European Alps as well as in Central Asia are included into the I component of the updated ESM (see Chapter 7).

Mass variability from LSDM in Antarctica and Greenland is masked out from LSDM results, since those effects are covered by the I component of the updated ESM. Further, all locations defined as ocean by the AOD1B land mask are also removed from the data-set. A time-mean terrestrial water storage field for the full period between 1995 and 2006 is calculated and removed in order to arrive at mass anomalies. The daily grids are subsequently interpolated to 6-hourly time-steps concurrent with ERA-Interim as the input for the spherical harmonics analysis step.

6.2 Characteristics of Component H

Linear trends in the H component of the updated ESM (Fig. 6.2) are generally small: they reach only a few cm equivalent water thickness (eq.w.th.) mostly in very humid regions and are generally coherent over larger areas. We rate those trends as in general rather smaller than in reality: antropogenic ground water extraction and irrigation are expected to cause substantial declines in the terrestrially stored water in various regions of the Earth. If a gravity mission candidate however suceeds in retrieving the small TWS trends contained in the updated ESM, it is likely to be able to trace the much stronger antropogenic effects.

The variability included in the H component is dominated by strong variations in water masses stored in the large surface water bodies as rivers or lakes (Fig. 6.3). Dominant signals occur in the Amazon basin, up to 40cm eq.w.th. along the main river channel, the Congo river, and to a little lesser extent at Ob and Lena. The simulated water management for the Aswan dam at the lower Nile leads to 35 cm eq.w.th. standard deviation in the Lake Nasser.

By separating the variability into periods longer and shorter (Fig. 6.4) than 30 days by applying a 3rd order Butterworth filter to the time-series of each grid point, we note that even though the hydrological variability is dominated by seasonal signals at periods longer than one month, in some regions sub-monthly variability of more than 1 cm eq.w.th. arises in the H component of the updated ESM. Those sub-monthly variability is particularly related to regions with strong episodic precipitation events that cause occasionally steep increases in the water storage. Since those signals

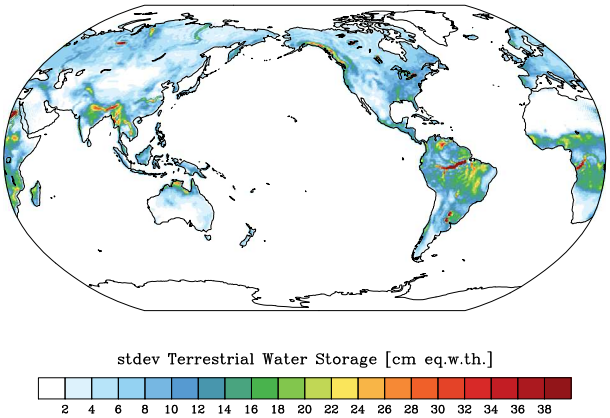

Figure 6.3: Standard deviation of terrestrial water storage anomaly (1995-2006) at 0.5° spatial resolution obtained from the re-synthesized and locally detrended coefficients of the H component from the updated ESM.

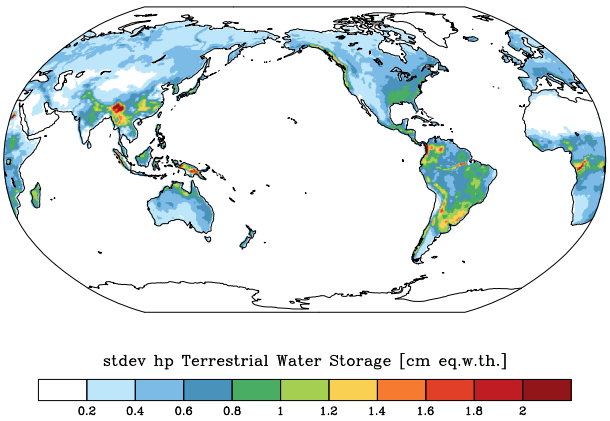

Figure 6.4: Standard deviation of terrestrial water storage anomaly (1995-2006) at 0.5° spatial resolution obtained from the re-synthesized, locally detrended and high-pass filtered (30 day cut-off) coefficients of the H component from the updated ESM.

might potentially contribute to aliasing errors, we believe it is important to have them included into the updated ESM.

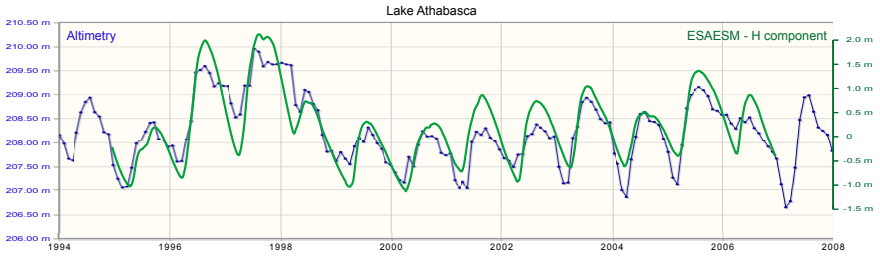

Figure 6.5: Altimetry vs. updated ESM for Lake Athabasca. Green line: TWS from ESAESM - H (only hydrological part from LSDM),blue line: lake level from Open Altimetry Data Base.

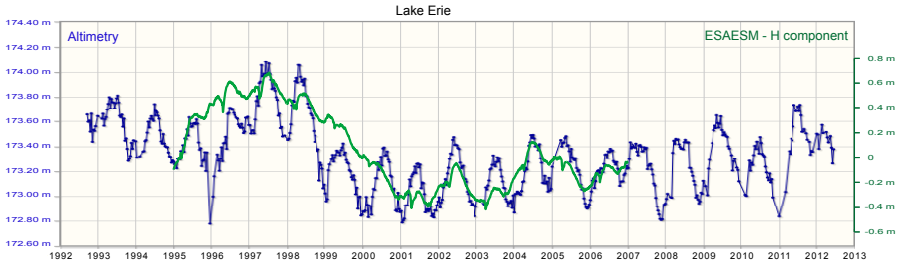

Figure 6.6: Altimetry vs. updated ESM for the Lake Erie. Green line: TWS from ESAESM - H (only hydrological part from LSDM), blue line: lake level from Open Altimetry Data Base.

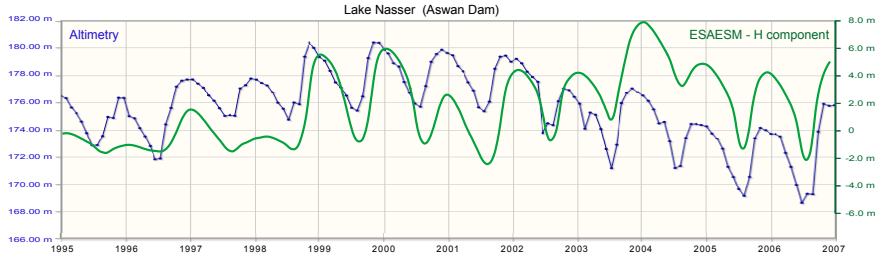

Figure 6.7: Altimetry vs. updated ESM for the Lake Nasser (Aswan Dam). Green line: TWS from ESAESM - H (only hydrological part from LSDM), blue line: lake level from Open Altimetry Data Base.

6.3 Validation with Satellite Altimetry over Surface Water Bodies

Modeled variations of terrestrial water storage in great lakes can be locally compared to time series of the lake surface height as derived from satellite altimetry and provided by the Database for Hydrological Time Series of Inland waters (DAHITI; Open Altimeter Database, http://openadb.dgfi.badw.de). Exemplarily, Fig. 6.5, 6.6, and 6.7 show the comparison of water storage variations of the H component of the updated ESM with satellite altimetry for different medium-scale lakes and the human-managed Lake Nasser indicating realistic seasonal and interannual variations in the updated ESM.

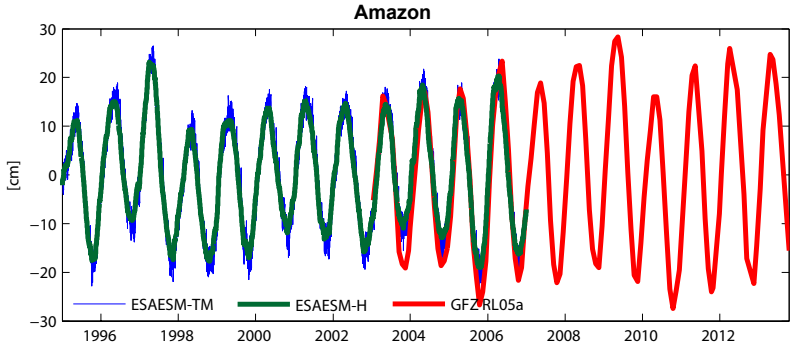

Figure 6.8: GRACE (GSM+GAC) vs. updated ESM for the Amazon basin. Blue line: updated ESM - AOHIS, green line: TWS from updated ESM - H (only hydrological part from LSDM), and red line: GRACE (GSM+GAC, i.e., including atmosphere and ocean).

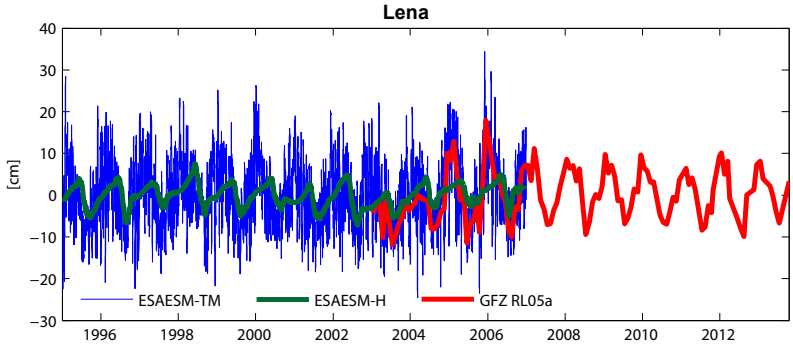

Figure 6.9: GRACE (GSM+GAC) vs. updated ESM for the Lena basin. Blue line: updated ESM - AOHIS, green line: TWS from updated ESM - H (only hydrological part from LSDM), and red line: GRACE (GSM+GAC, i.e., including atmosphere and ocean).

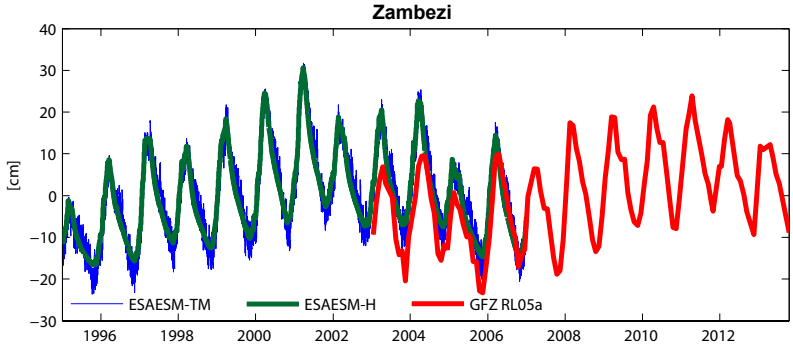

Figure 6.10: GRACE (GSM+GAC) vs. updated ESM for the Zambezi basin. Blue line: updated ESM - AOHIS, green line: TWS from updated ESM - H (only hydrological part from LSDM), and red line: GRACE (GSM+GAC, i.e., including atmosphere and ocean).

6.4 Validation with GRACE

Regional variations of terrestrial water storage in the H component of the updated ESM can be compared to total mass variations derived from GRACE observations, regionally filtered by appropriate basin functions. Figures 6.8, 6.9, and 6.10 give the basin-wide total mass variation in cm eq.w.th. observed by GRACE (GSM + GAC, i.e., including atmosphere and ocean) and the comparable total mass variation in the updated ESM (AOHIS). Additionally, the contribution of terrestrial hydrology alone (H component) is given. The Amazon and Zambezi basins are dominated

by the hydrological signal with well matching amplitudes of the seasonal and interannual variations between the GRACE observation and the updated ESM. Typically for catchments in high northern latitudes, the Lena basin shows equal contributions from seasonal atmospheric and hydrological variations overlaid by high-frequency atmospheric variability. Interannual variations caused by the time delay between soil moisture contributions, appearing in phase with atmospheric variations, and the accumulation and melting of snow are captured well by the updated ESM. Future gravity mission might be tested to resolve sub-monthly phase differences in TWS between different storage compartments (soil moisture, snow, rivers, lakes) located close together in one river basin.

Chapter 7

Continental Ice-Sheets and Mountain Glaciers

7.1 RACMO2 Surface Mass Balance, Ice-Discharge, and Glacier Mass Balance

The regional climate model RACMO2 (Ettema el al., 2009) provides high-resolution estimates of individual components of the surface mass balance - precipitation, evaporation and sublimation, run-off, melting and re-freezing - of glaciated regions in both Greenland and Antarctia. The model is forced at its lateral boundaries and at the sea-surface with the ECMWF re-analysis ERA-Interim, and runs at a spatial resolution of 11 km. Daily surface mass balance estimates are available from recent RACMO simulations for the period 1995 - 2006.

Besides by accumulated surface mass balance, the low frequency ice mass balance is in particular determined by the ice dynamics, which transports masses laterally towards the oceans. Since reliable numerical model simulations for both Antarctica and Greenland where not readily available to us for the updated ESM, we approximate ice dynamics by estimating the slowly varying ice mass changes - i.e., the local secular trends and the lowpass filtered signals at periods longer than 1000 days - from the re-synthesized original ESM (Gruber *et al.*, 2011), with a long-term mean subtracted, and an ocean mask applied in order to exclude spurious leakage artifacts in oceanic regions. Note that signals at similar frequencies are removed from the RACMO estimates prior to the combination in order to avoid double book-keeping effects.

Ice mass balance for mountain glaciers and isolated ice-caps is not simulated dynamically, but is instead only included by means of linear trends for four groups of glaciers in Alaska, the European Alps, the Himalaya, and the Karakoram Mountain Range. Areas and loss rates imposed follow the suggestions given by Gruber *et al.* (2011), but have been re-calculated based on globally gridded data obtained from the World Glacier Inventory.

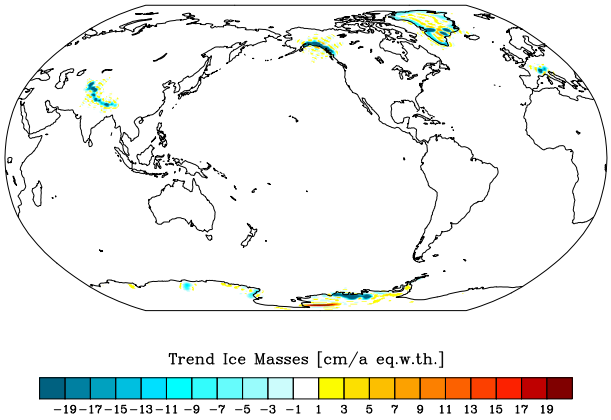

Figure 7.1: Local secular trends (1995-2006) at 0.5° spatial resolution obtained from the re-synthesized coefficients of the I component from the updated ESM.

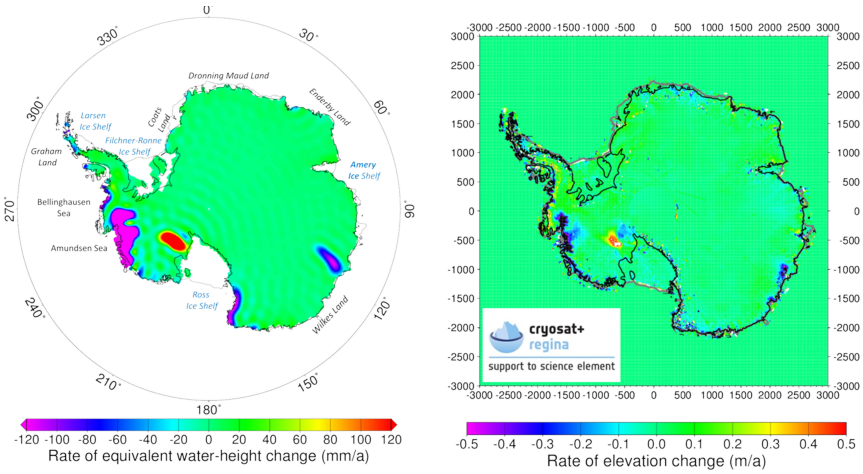

Figure 7.2: Rate of equivalent water-height change of the updated ESM (1995–2006) and rate of elevation change from a combination of Envisat/ICESat data (2002–2009), courtesy of STSE project REGINA, www.regina-science.eu, for Antarctica. The main regions with negative and positive mass change rates are captured in the updated ESM, however, with a smoothed spatial resolution.

7.2 Characteristics of Component I

Figure 7.1 shows the linear trend in the updated ESM component I estimated for the time period 1995–2006. The signal for Antarctica is shown in Fig. 7.2. For comparison, the rate of elevation change obtained from a combination of ICESat/Envisat for 2003-2009 is given (courtesy of ESA STSE project REGINA, www.regina-science.eu). It is visible that the updated ESM captures the main "hot spots" of ice dynamic imbalances, e.g. the mass loss in the Amundsen Sea Embayment, the increase in mass of the Kamb ice stream, which has been thickening in the recent past, as well as mass loss along the Antarctic Peninsula. Similarly, the mass losses of the ESA ESM for the Greenland ice sheet (Fig. 7.3) match well with the locations of strong negative rates of elevation change observed with ICESat (Sørensen *et al.*, 2011), e.g. the Jacobshaven ice stream in West Greenland and the Helheim glacier in East Greenland.

It should be noted that the long-term component relies on the original version of the ESM (Gruber *et al.*, 2011), with a loss in resolution due to the spherical-harmonic truncation at d/o = 180. Also, the mass anomalies for different glacier systems regions show a synchronous behaviour. Although this captures the main magnitudes and locations of ice-dynamic mass loss, as

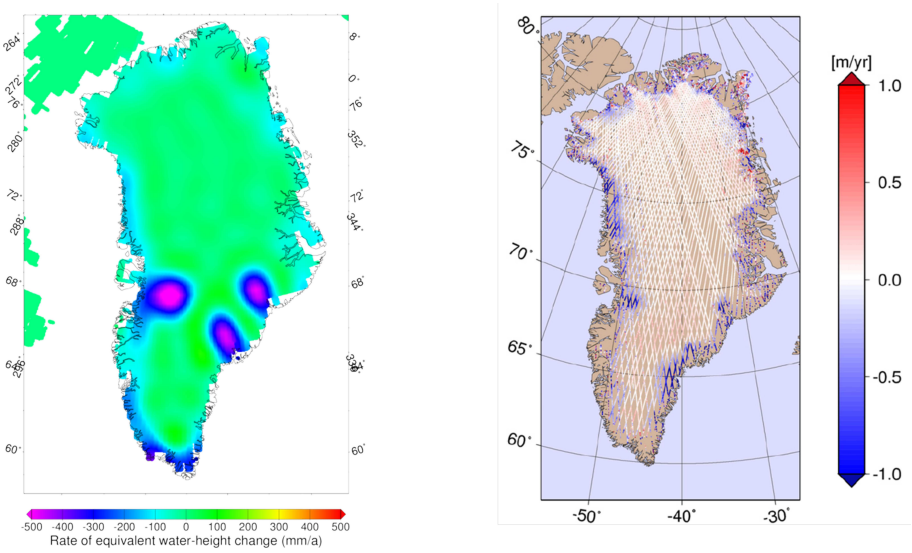

Figure 7.3: Rate of equivalent water-height change of the updated ESM (1995–2006), left, and rate of elevation change ICESat data (2002–2009; Sørensen *et al.* (2011)), right, for Greenland. Ice-dynamic imbalances of the large glacier systems are represented, despite with coarse spatial resolution, as well as the increased mass loss along the ice sheet margin due to stronger melt production.

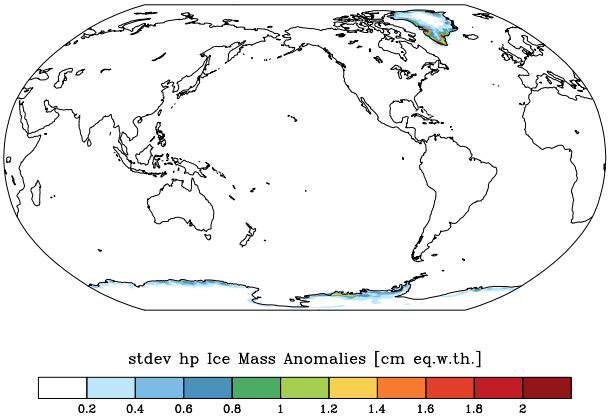

Figure 7.4: Standard deviation of ice-mass anomaly (1995-2006) at 0.5° spatial resolution obtained from the re-synthesized, locally detrended and high-pass filtered (30 day cut-off) coefficients of the I component from the updated ESM.

well as the increase in melt production along the margin of the Greenland ice sheet, refinements are possible on, for example, including mass fluctuations of individual glaciers and also by including a more complex temporal behaviour. This would increase the realism of the simulation based on the updated ESM, as individual neighboring glacier systems tend to behave rather differently on the time scale of a decade. Nevertheless, it is considered that the current assemblage of the updated ESM covers the spatial and temporal scales with sufficient extent.

7.3 Validation with GRACE

Inter-annual down to monthly mass variations of the polar ice sheets are dominated by variations in the surface mass balance (Fig. 7.4). For Antarctica (Fig. 7.5), these variations are mainly caused by fluctuations in the net accumulation to the ice sheet. For Greenland, also net run-off, i.e. the

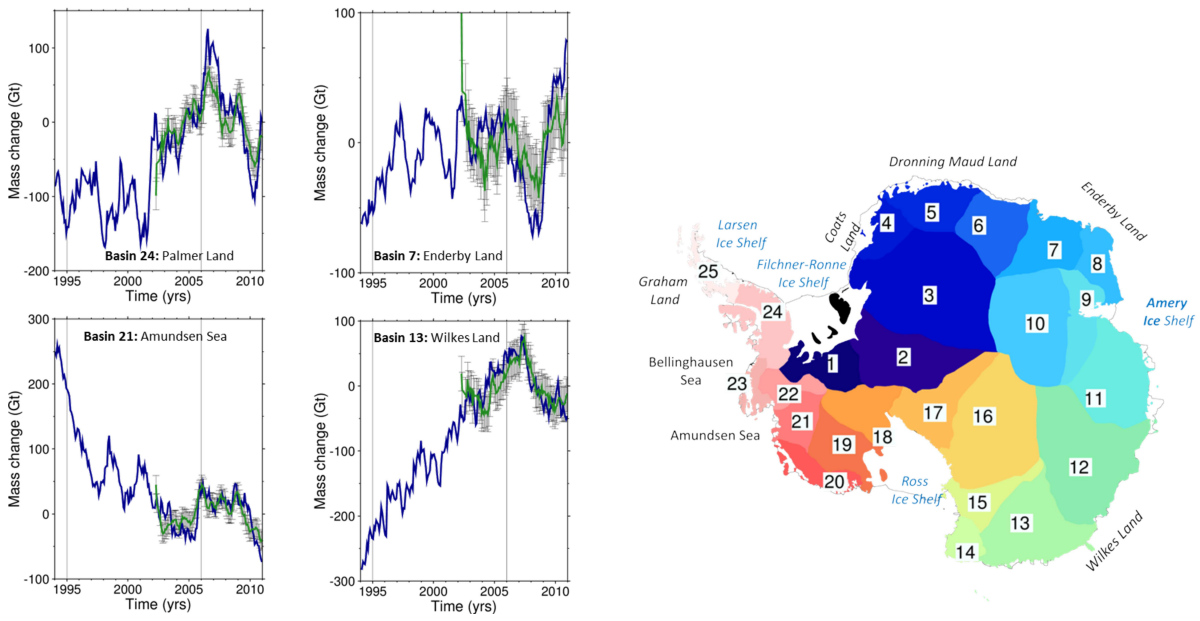

Figure 7.5: Comparison of interannual mass variations in Antarctica from RACMO2/ANT and GRACE (CSR RL05; Sasgen *et al.* (2013)), w.r.t. the period 2003-2010. Shown are selected time series for four basins with strong interannual mass variations and a high level of agreement between RACMO2/ANT and GRACE (left) and their geographic location (right).

difference between melting and re-freezing, plays an important role, leading to considerable year to year perturbations of the ice sheet's mass balance.

The interannual mass variations in component I of the updated ESM presented here are based on output of RACMO2/ANT (Antarctica) and RACMO2/GR (Greenland). RACMO2/GR has been validated with GRACE data for the entire Greenland ice sheet (van den Broeke *et al.*, 2009), as well as for its subdivision into seven major drainage basins (Sasgen *et al.*, 2012). The calculations rely on computing the mass anomalies w.r.t. the climatological reference period of the years 1960–1990, for which the imbalance of the ice sheet is assumed to be zero.

For Antarctica, the situation is more complicated, as meteorological time series do not extend as long backwards in time as for Greenland, hampering the definition of a meaningful climatological reference period for RACMO2/ANT. However, the simulations employed for the updated ESM encompass the period 1979–2010, showing eight years of overlap with the GRACE measurements. Therefore, to validate the interannual variations in RACMO2/ANT we calculate the de-trended cumulative mass anomalies and compare them the the de-trended anomalies for the GRACE data for 25 basins of the Antarctic ice sheet.

Figure 7.5 shows the time series of monthly interannual mass variations for GRACE and RACMO2/ANT w.r.t. the common time period of the years 2003-2010, for four selected Antarctic drainage basin. Both time series reveal substantial interannual fluctuations in the mass of the ice sheet, primarily driven by accumulation variations. To reduce short-frequency noise in the GRACE data, the time series were smoothed with a 6-month moving average filter. For these basins, which lie in areas of strong atmospheric moisture flux onto the continent, the agreement between RACMO2/ANT and GRACE is very good, showing zero-order correlations of 0.6 or higher. Three basins (1, 6 and 23; not shown) also show correlations above 0.6. However, basins exhibiting lower interannual mass fluctuations show less agreement; the correlation coefficient of seven basins lies in the range between 0.3 and 0.6, and the remaining nine basins below 0.3.

Note that the interannual variations underlying the updated ESM are referenced to the time period 1995-2006 (not 2003–2010, as for the comparison with GRACE); both for Greenland and the Antarctic ice sheet, the RACMO2-based component of updated ESM describes cumulative anomalies of the surface-mass balance with respect to the mean surface-mass balance 1995-2006.

Chapter 8

Glacial Isostatic Adjustment and Co- and Post-Seismic Deformations

8.1 Repatching of the Earth Quake Model

The solid Earth part of the original Earth System Model (Gruber *et al.*, 2011) is composed of three distinctly different signals: (i) local secular trends due to glacial isostatic adjustment (GIA) that is considered as linear over the period 1995 - 2006, (ii) a co-seismic deformation associated with the magnitude 9.1 Sumatra-Andaman Earth Quake between Dec 26, 00:00 and 06:00, that is followed (iii) by linearly increasing post-seismic deformation lasting over 365 days. Those signals contained in the original ESM are generally found to be realistic and sufficiently detailed for modern satellite gravimetry simulation studies, except for strong Gibbs effects that arise from the edges of the Earth Quake model domain that has been patched into the GIA trends rather poorly.

To isolate co- and postseismic deformation from the GIA signals, we synthesize the original ESM onto a global grid and estimate and remove the long-term mean value at each location. Subsequently, we (i) estimate the GIA trend contained in the original ESM from the period 1995 - 2004, and remove it from the whole period 1995 - 2006, followed by (ii) an estimation and removal of the post-seismically induced trend in the year following the main shock. Finally, (iii) the co-seismic deformation is calculated from the difference of the remaining residuals before and after the seismic event.

Edges of both trend and offset pattern obtained are then smoothed with a nine-point spatial averaging kernel in order to reduce the Gibbs effects, and time-changes in C_{00} are removed by adjusting the global mean of the obtained individual anomalies. The thereby obtained modified solid Earth components are again added together in the spacial domain before analyzing them back into spherical harmonics.

8.2 Coefficients of Degree 1

The contribution of GIA to the degree 1 components was missing in Gruber *et al.* (2011) due to their representation of this component in the CE system (referenced to redistribution of internal masses only). In the updated ESM, the fields are represented in the CF system (see Sec. 2.2), meaning the degree 1 component due to GIA has to be predicted by independent means. We employ the geocenter motion presented in Klemann & Martinec (2011), which is calculated for a standard incompressible viscoelastic solid-earth structure, and from which the respective potential

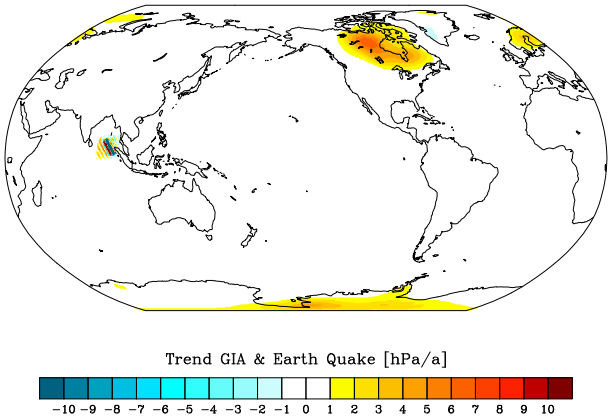

Figure 8.1: Local secular trends (1995-2006) at 0.5° spatial resolution obtained from the re-synthesized coefficients of the S component from the updated ESM.

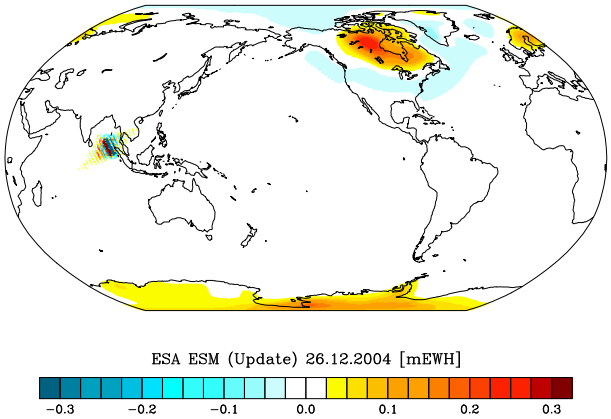

Figure 8.2: Coseismic signal at 0.5° spatial resolution obtained from the updated ESM.

coefficients (Kusche, 2010) are derived:

$$c_{10} = \sqrt{\frac{1}{3}}\, x_3 \,, \quad c_{11} = \sqrt{\frac{1}{3}}\, x_1 \,, \quad s_{11} = \sqrt{\frac{1}{3}}\, x_2 \,. \tag{8.1}$$

where $x_{[123]}$ are the cartesian components of the predicted geocenter motion.

8.3 Characteristics of Component S

The characteristics of the component S is largely unchanged with respect to Gruber *et al.* (2011), where the signal in the linear trend clearly reveals the uplift of the formerly glaciated regions of Laurenia and Fennoscandia, and the prominent signal in West Antarctica (Fig. 8.1). The trend determined for the Sumatra region is artificial as it mainly represents the discontinuous co-seismic signal (see Fig. 8.2).

In the detrended signal, the GIA contribution vanishes due to the fact that, on the considered time scale of 10 years, there is no deviation from a linear trend (Fig. 8.3) and the co- and post-seismic signal remains.

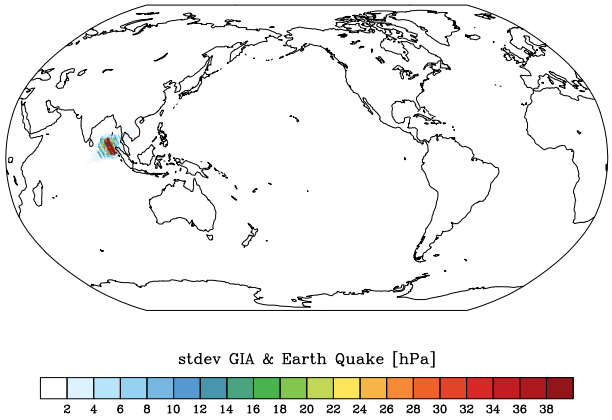

Figure 8.3: Standard deviation of solid-earth effects (1995-2006) at 0.5° spatial resolution obtained from the re-synthesized and locally detrended coefficients of the S component from the updated ESM.

Chapter 9

Characteristics of AOHIS

9.1 Combination Strategy

Spherical harmonics have been analysed individually for each of the components A, O, H, I, and S of the updated ESM. Since the sum of all components is usually required as input for the orbit computions in a satellite mission simulation set-up, we add those individual components in the spectral domain and provide the sum under the label 'AOHIS' additionally to the individual components.

9.2 Characteristics of AOHIS

While analyzing the AOHIS coefficients, we note slight variations in the total mass as reflected by the coefficient C_{00} (Fig. 9.1). Fluctuations show systematic effects that correspond to changes in total ocean mass both on seasonal time-scales and in the long-term trend. The magnitude of those fluctuations is, however, about 3 orders of magnitude smaller than the eustatic sea-level variations, and can be therefore safely neglected.

Global trend pattern of AOHIS are dominated by GIA signals at the position of the former Laurentide Ice-sheet as well as over Fennoscandia and in the Antarctic (Fig. 9.2). In addition, ice mass changes in both the continental ice-sheets and mountain glaciers are present. Hydrological trends

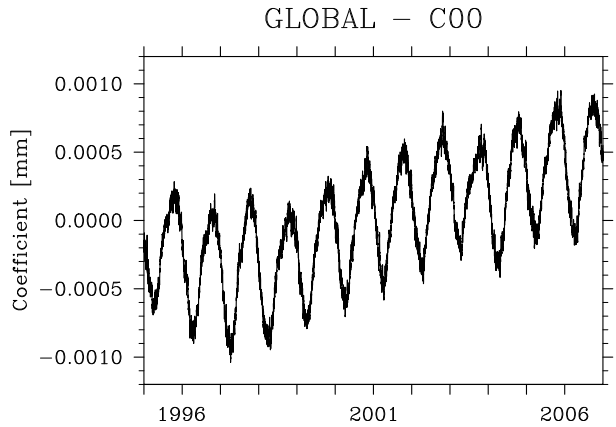

Figure 9.1: Global mass conservation of the updated ESM, C00 coefficient (1995 - 2006).

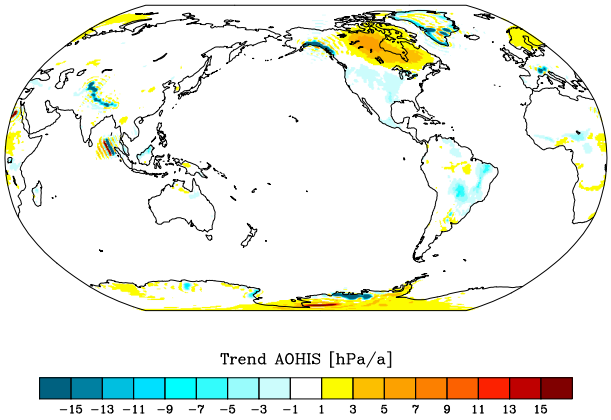

Figure 9.2: Local secular trends (1995-2006) at 0.5° spatial resolution obtained from the re-synthesized coefficients of the AOHIS component from the updated ESM.

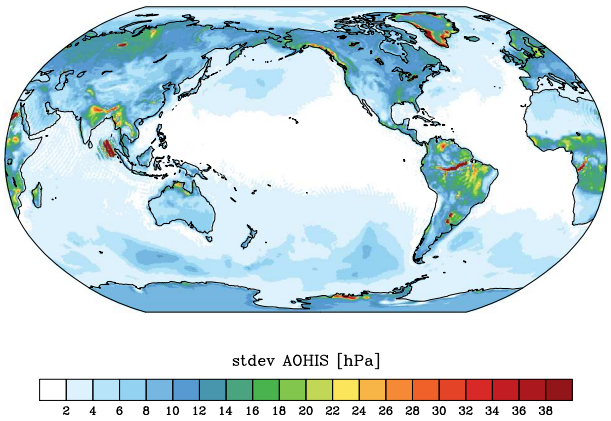

Figure 9.3: Standard deviation of total pressure anomaly (1995-2006) at 0.5° spatial resolution obtained from the re-synthesized and locally detrended coefficients of the AOHIS component from the updated ESM.

are less dominant, but still large enough to be possibly detected from a simulation scenario of a third generation gravity mission.

Total (Fig. 9.3) and low-frequency variability (Fig. 9.4) is dominated by variations in terrestrial water storage, steepest spatial gradients are associated with surface water stored in rivers or lakes. In addition, we note ocean-bottom pressure signals that are substantially smaller than the continental signals, as well as effects of the Sumatra Andaman co- and post-seismic deformation, that also contribute to the rms values shown here.

High-frequency variability (Fig. 9.5) instead is dominated by atmospheric mass variability and corresponding ocean bottom pressure signals in response to the time-varying winds. Here, it is in particular important to note once more that in tropical latitudes, almost no high-frequency variability is present, as long as sub-diurnal signals and atmospheric tides are excluded.

9.3 Validation of Low-Degree Spherical Harmonics

In contrast to the original ESA ESM, the updated model version does also provide estimates of the spherical harmonic coefficients with d = 1. Degree-1 coefficients for the combined model AOHIS (Fig. 9.6) are compared against estimates from Satellite Laser Ranging and a joint inversion of a global GPS network solution, GRACE terrestrial mass anomalies, and ocean-bottom pressure

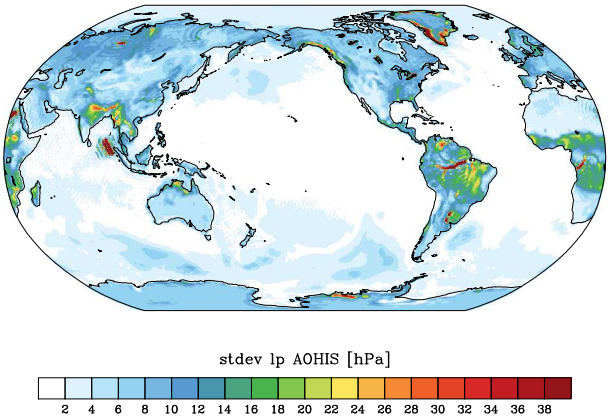

Figure 9.4: Standard deviation of total pressure anomaly (1995-2006) at 0.5° spatial resolution obtained from the re-synthesized, locally detrended and low-pass filtered (30 day cut-off) coefficients of the AOHIS component from the updated ESM.

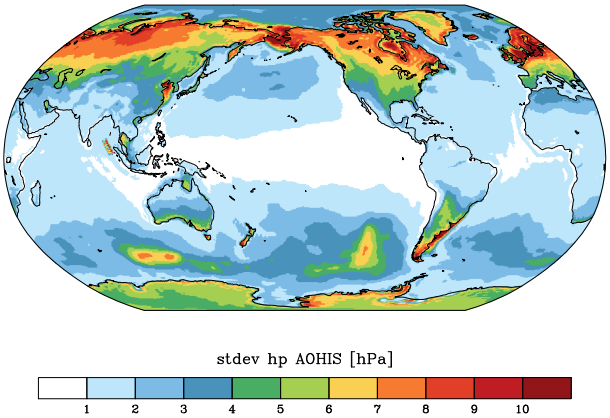

Figure 9.5: Standard deviation of total pressure anomaly (1995-2006) at 0.5° spatial resolution obtained from the re-synthesized, locally detrended and high-pass filtered (30 day cut-off) coefficients of the AOHIS component from the updated ESM.

from a global numerical model (Rietbroek *et al.*, 2009). Variability on annual periods and shorter are similar between AOHIS and the joint inversion, whereas the SLR solution exhibits stronger month-to-month variability. Long-term trends, however, are apparently not included in the joint inversion, but show up in the SLR solution with a substantial decline in C_{10}. AOHIS also contains such a decline, albeit at a smaller rate. This feature is due to the inclusion of the solid Earth degree-1 trends following Klemann & Martinec (2011) into AOHIS.

For degree-2, we also find realistic variability in AOHIS when compared to SLR results (Fig. 9.7). Both amplitudes and phases are generally comparable when monthly mean values are contrasted against each other. In addition, trends in degree-2 coefficients of AOHIS are consistent with SLR as well.

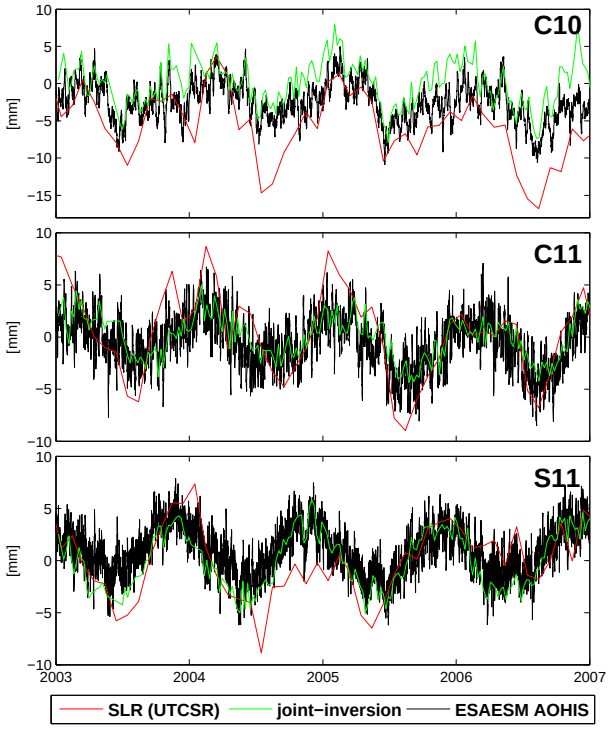

Figure 9.6: Degree-one coefficients C10, C11, S11 (2003 - 2006) of the updated ESM (black), from SLR UTCSR (red) and a joint inversion (green).

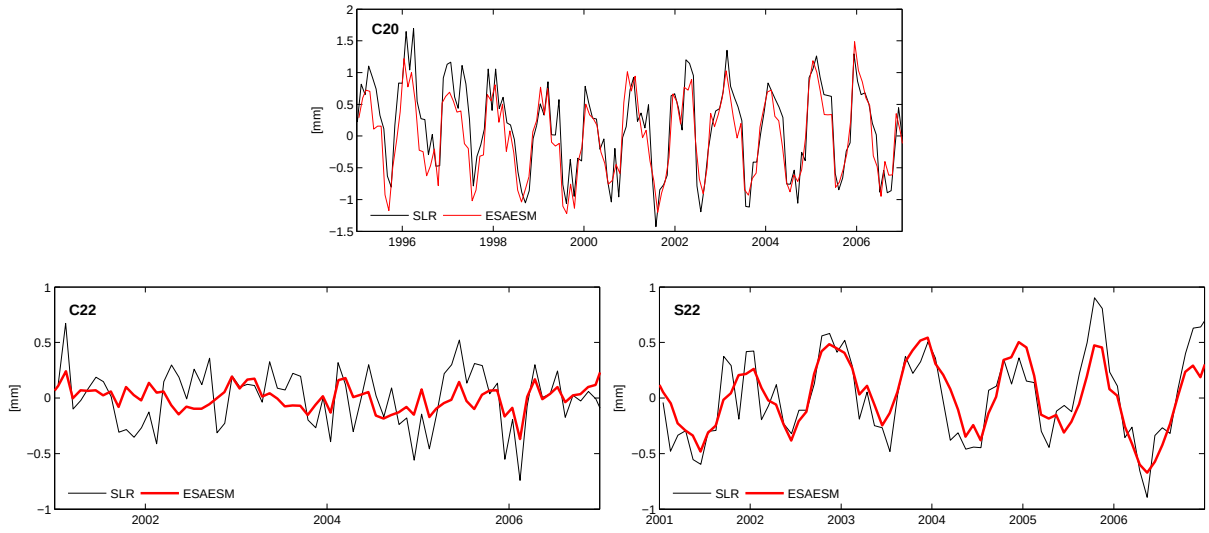

Figure 9.7: Degree-two coefficients C20, C22, S22 (1995 - 2006) of the updated ESM (red) and from SLR (black).

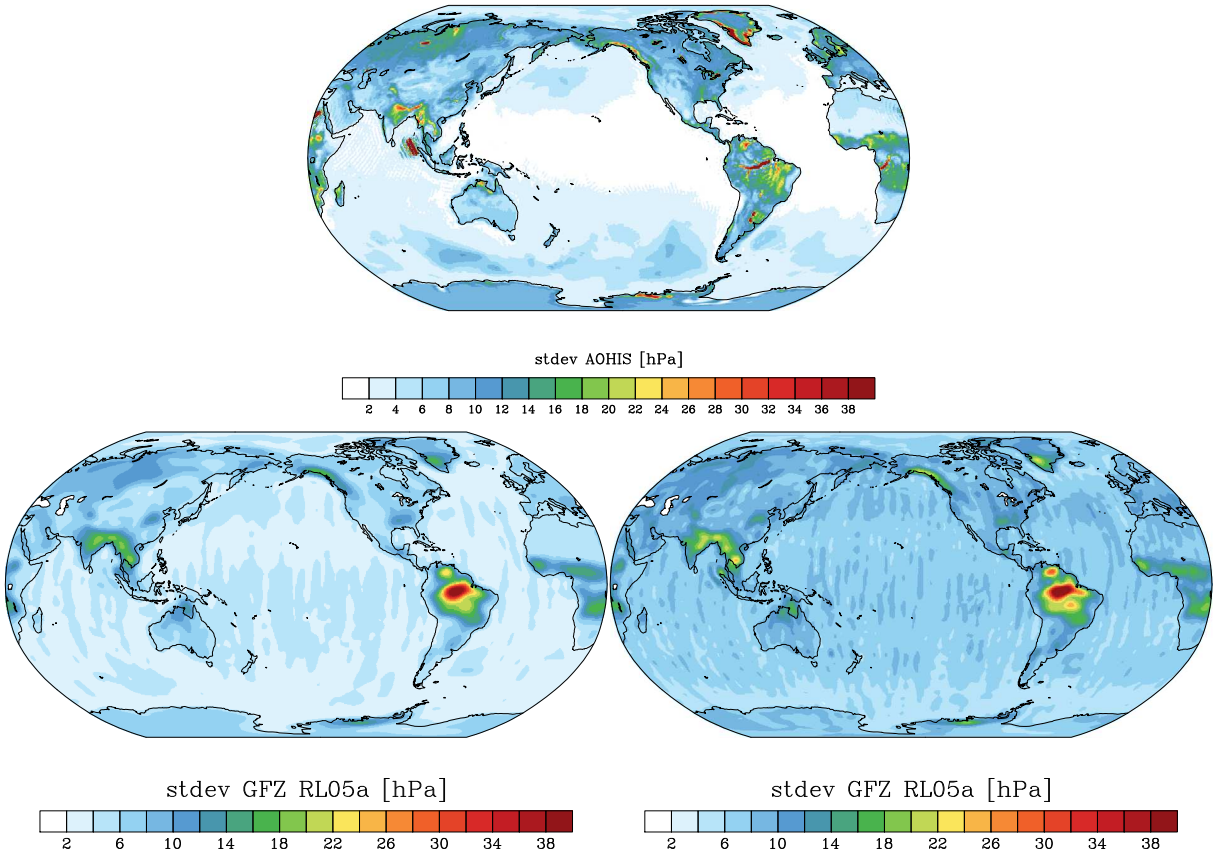

Figure 9.8: Standard deviation (1995 – 2006) of the updated ESM (top), GRACE GFZ RL05a filtered with DDK3 (left) and GRACE GFZ RL05a filtered with DDK5 (right).

9.4 Validation of Regional Mass Variability

We also perform a brief comparison of the de-trended monthly mean mass anomalies of AOHIS with GRACE (Fig. 9.8). Variability levels in all places in the world are generally comparable, and tend to converge to the places with strongest signal amplitudes when spatial smoothing of GRACE estimates is reduced by applying DDK5 instead of DDK3. For one particular monthly solution in March 2006 (Fig. 9.9), we note a close correspondence of the pattern shown by both AOHIS and GRACE in terms of large-scale signals. But in addition to those large-scale variabilities, AOHIS of the updated ESM contains a vast range of small-scale variations currently not detectable by GRACE, which are all potential target signals that a next generation gravity mission might search for.

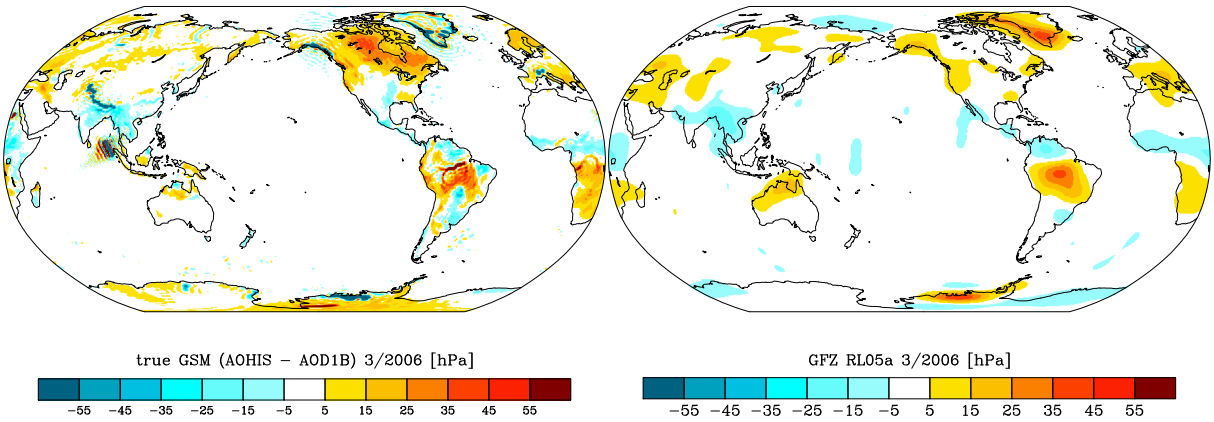

Figure 9.9: True GSM signal for March 2006: updated ESM AOHIS - AOD1B (left) and GRACE GFZ RL05 (right).

Chapter 10

Tides and Sub-Diurnal Atmospheric and Oceanic Variability

10.1 Atmospheric Tides

In contrast to the lunisolar gravitational tides, atmospheric tides or so-called air tides are caused by daily varying solar insolation that is absorbed by water vapour and ozone in different height levels of the atmosphere. Changes in temperature and corresponding adjustments in the pressure and wind fields excite waves that propagate both, laterally and horizontally, and thereby cause periodic variability at the corresponding tidal frequency all around the globe.

In addition, tidal variations in atmospheric surface pressure cause periodic surface loads on the ocean surface that trigger also waves in the water at identical frequencies. Here, we treat atmospheric tides and their oceanic response in combination. Since air tides are principally caused by the diurnal cycle of the solar insolation, they occur at periods of 24 h and higher harmonics of it. Since the Nyquist period for a 6 hourly sampled data-set corresponds exactly to the period of the semi-diurnal air tide S2(p), it partially aliases into a standing wave pattern. Consequently, S2(p) signal parts are removed from the updated ESM, leaving only S1(p) tidal signals to discuss here.

From the 6 hourly ERA Interim analyses, S1(p) is sampled at exactly the same phase every day. Its characteristics are therefore conveniently described by the mean tidal signal at the time-steps 00:00, 06:00, 12:00, and 18:00 UTC (Fig. 10.1). We find small-scale signals of about 1.5 hPa over the continents, where local atmospheric processes are of great relevance for the S1(p) surface pressure signal. Over the oceans, the fields are dominated by the oceanic response wave, with highest amplitudes at the coasts of the largest ocean basins. In addition, we identify strong signals in enclosed seas as the Gulf of Carpentaria, whose bathymetric characteristics make the basin resonant or near-resonant to variations at 24 h periods.

10.2 Sub-Diurnal Variability

By subtracting daily running means from the sum of A+O of the updated ESA ESM, we finally arrive at a time-series containing only sub-diurnal variability. Note that signals at the tidal frequency S1(p) are removed in order to avoid a double book-keeping here. The spatial pattern of variability (Fig. 10.2) is dominated by coastal signals in the oceans that reach up to 5 hPa. In addition, also some variability of about 2 hPa is visible in North America or Central Russia.

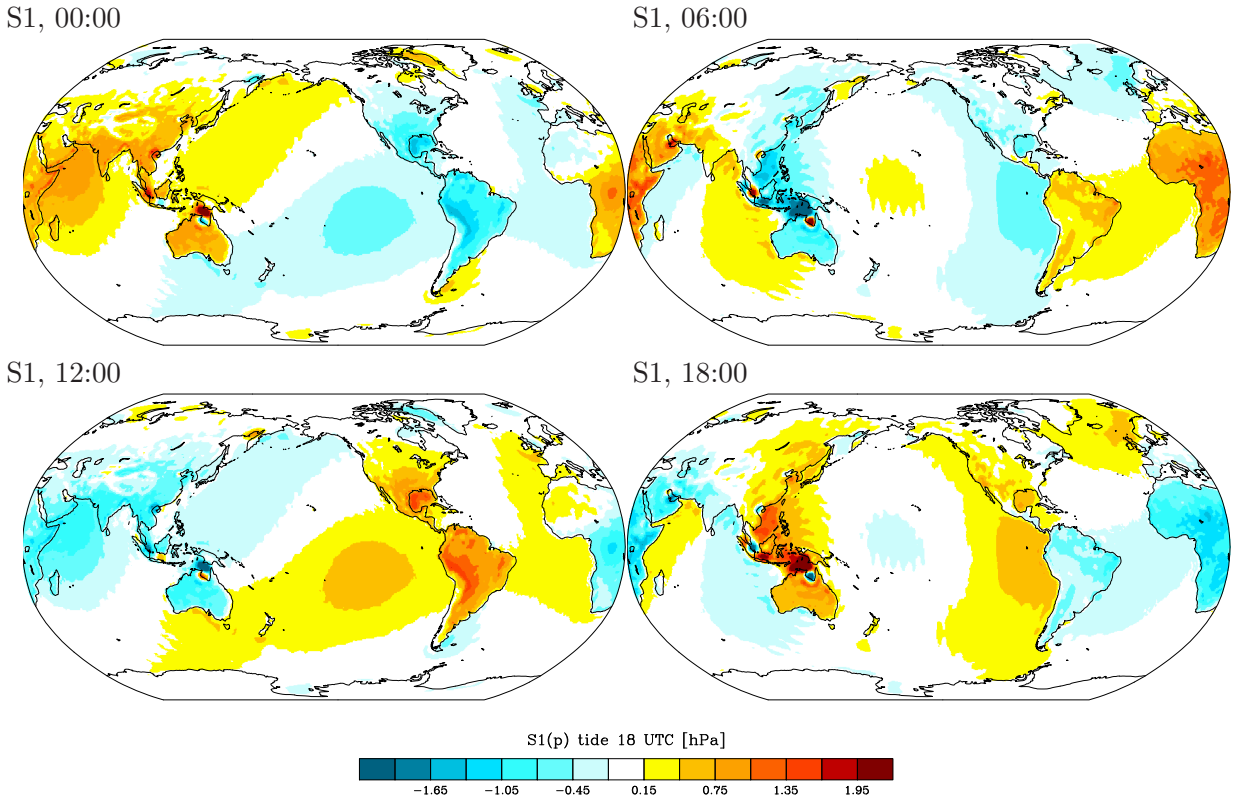

Figure 10.1: Characteristics of the mean atmospheric tide S1(p) and its corresponding response at 00:00, 06:00, 12:00, and 18:00 UTC as included in the sum of the components A and O of the updated ESM averaged over 1995 - 2006.

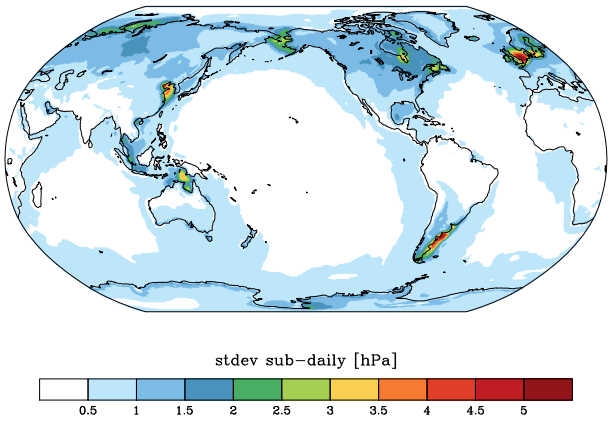

Figure 10.2: Variability at periods shorter than 24 hours in the sum of the components A and O of the updated ESM over the years 1995 - 2006.

Chapter 11

Effects of Higher Spatial and Temporal Resolution

11.1 Effects of Increased Spatial Resolution

For the year 2006, additional high-resolution data-sets that are analysed until d/o = 360 are available within the updated ESM. Those high-resolution data-sets are down-sampled to 6 hours, and subsequently re-synthesized onto a global grid in two variants: up to d/o = 180, and up to d/o = 360. Rms values of the differences of both variants for the components A and Ac (Fig. 11.1) indicate that small-scale variations of up to 5 hPa are visible along the coasts, where discontinuities in atmospheric pressure due to the applied IB-correction are strongest. Numerical experiments with a full-scale simulation set-up might help to analyse if such signals at very small spatial scales have a relevance for a next generation gravity mission.

Comparable analyses are also performed for the components O, H, and I (Fig. 11.2). Note that since the solid Earth component of the updated ESM is essentially the same as in the original ESM, no signals at higher spatial scales are available, since the original ESM was only delivered until d/o = 180. For the oceans, we note small-scale signals in particular in the Southern ocean, where the high-resolution MPIOM STORM experiment provides very detailed ocean bottom pressure patterns. For the terrestrially stored water, the discontinuities of TWS along the boundaries of the surface water bodies contribute to substantial spatial leakage, which might be close to the

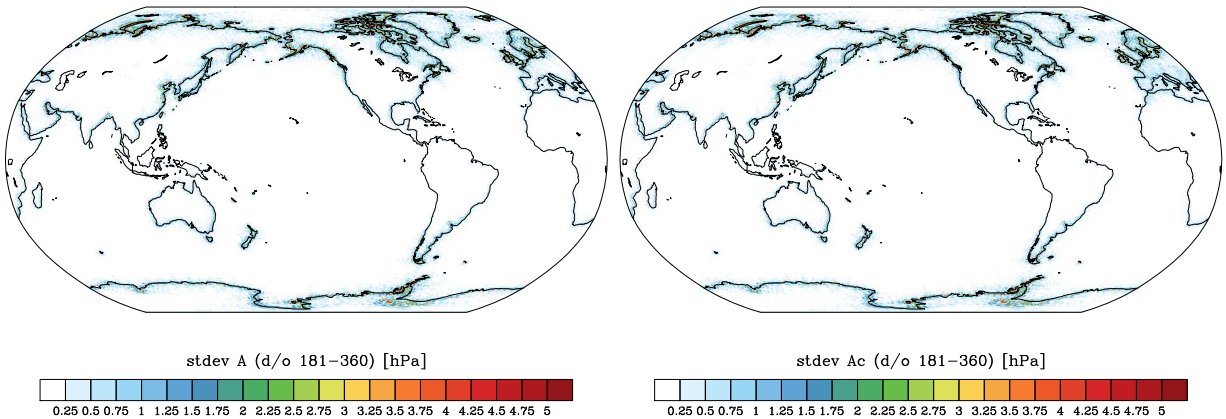

Figure 11.1: Variability at small spatial scales (d/o = 181 ... 360) in updated ESM A (left) and Ac (right) components averaged over the years 1995-2006.

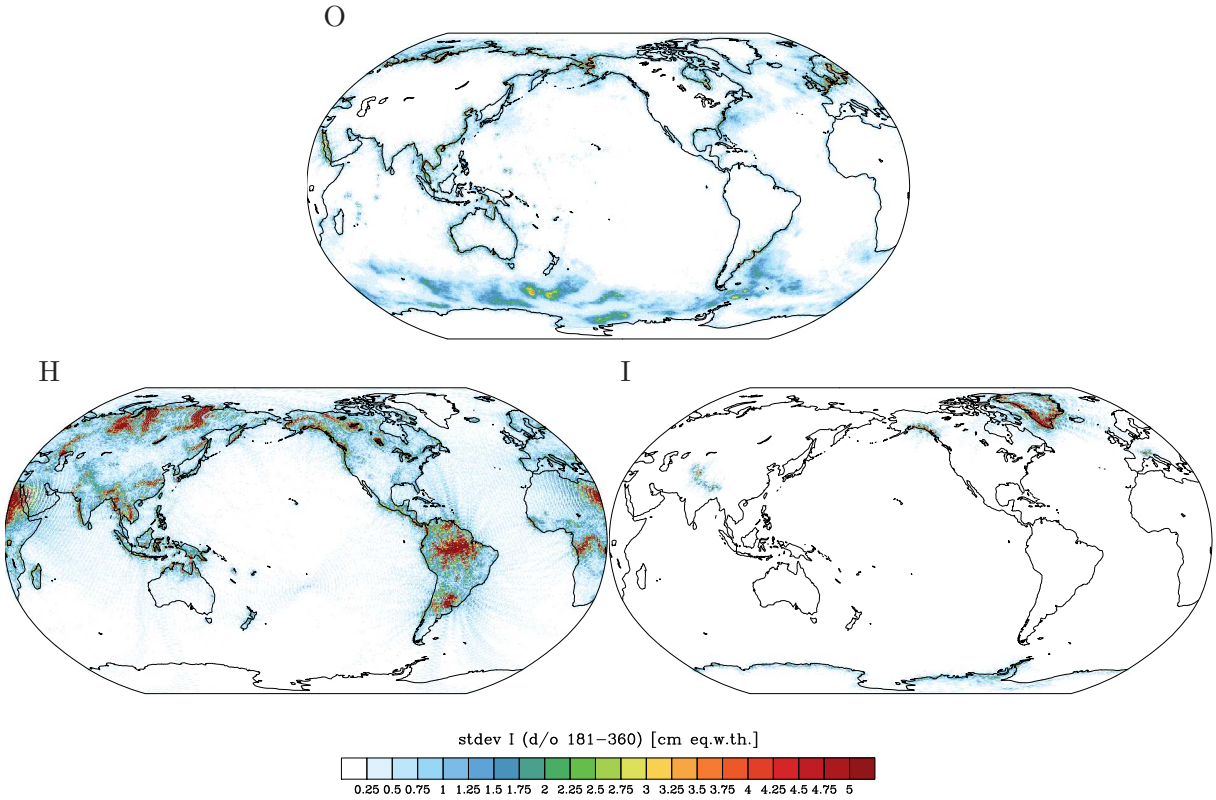

Figure 11.2: Variability at small spatial scales (d/o = 181 ... 360) in updated ESM O (top), H (left), and I (right) components averaged over the years 1995-2006.

sensitivity threshold of a next generation gravity mission. Similar conclusions are obtained for the I component.

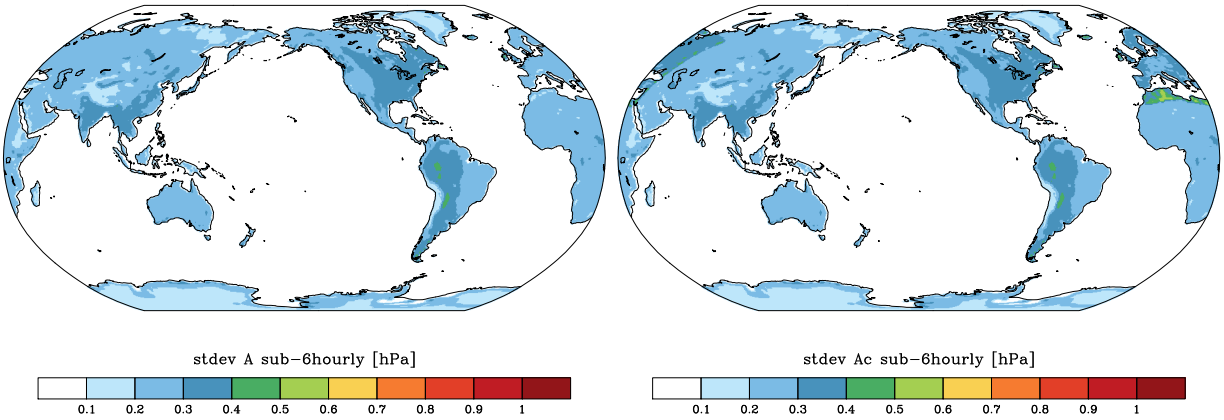

Figure 11.3: Variability in A component (left) and Ac component (right) not solved by the 6 hourly sampled updated ESM.

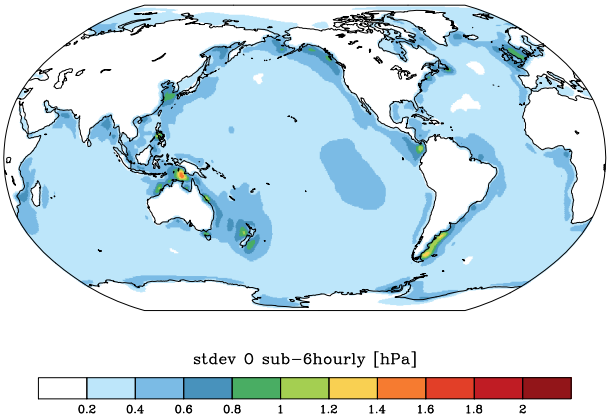

Figure 11.4: Variability in O component not solved by the 6 hourly sampled updated ESM.

11.2 Effects of Increased Temporal Resolution

In addition to the higher spatial resolution, the updated ESM also provides for the year 2006 data at an increased temporal resolution of 3 hours. Whereas this increased resolution does not provide additional information for H, I, and S, since the geophysical source models used as a basis for those components are sampled daily only, we identify high-frequency variability in the atmosphere (Fig. 11.3) and the ocean (Fig. 11.4) with rms values of about 0.5 hPa. Again, sensitivity experiments with a full-scale simulation set-up might help to analyse if such signals at very small temporal scales indeed have a relevance for a next generation gravity mission.

Bibliography

Bergmann-Wolf, I., Dill, R., Forootan, E., Klemann, V., Kusche, J., Sasgen, I. & Dobslaw, H. (2014a). *Updating ESA's Earth System Model for Gravity Mission Simulation Studies, 2. Comparison with the Original Model, STR 14/08*, GFZ Potsdam, Potsdam, doi:10.2312/GFZ.b103-14088. 3

Bergmann-Wolf, I., Zhang, L. & Dobslaw, H. (2014b). Global eustatic sea-level variations for the approximation of geocenter motion from grace, *J. Geod. Science*, **4**, 37–48, doi:10.2478/jogs-2014-0006. 35

Blewitt, G. (2003). Self-consistency in reference frames, geocenter definition, and surface loading of the solid Earth, *J. Geophys. Res.*, **108**, doi:10.1029/2002JB002082. 18

Dee, D. P., Uppala, S. M., Simmons, A. J., Berrisford, P., Poli, P., Kobayashi, S., Andrae, U., Balmaseda, M. A., Balsamo, G., Bauer, P., Bechtold, P., Beljaars, A., Van De Berg, L., Bidlot, J., Bormann, N., Delsol, C., Dragani, R., Fuentes, M., Geer, A. J., Haimberger, L., Healy, S. B., Hersbach, H., Hólm, E. V., Isaksen, L., Kå llberg, P., Köhler, M., Matricardi, M., McNally, A. P., Monge-Sanz, B. M., Morcrette, J. J., Park, B. K., Peubey, C., De Rosnay, P., Tavolato, C., Thépaut, J. N. & Vitart, F. (2011). The ERA-Interim reanalysis: configuration and performance of the data assimilation system, *Q. J. Roy. Met. Soc.*, **137**, 553–597, doi:dx.doi.org/10.1002/qj.828. 21

Dill, R. (2008). *Hydrological model LSDM for operational Earth rotation and gravity field variations Hydrological model LSDM for operational Earth rotation and gravity field variations, STR 08/09*, GFZ Potsdam, Potsdam, doi:11.2312/GFZ.b103-08095. 39

Dill, R. & Dobslaw, H. (2010). Short-term polar motion forecasts from earth system modeling data, *J. Geodesy*, **84**, 529–536, doi:10.1007/s00190-010-0391-5. 39

Dill, R. & Dobslaw, H. (2013). Numerical simulations of global-scale high-resolution hydrological crustal deformations, *Journal of Geophysical Research: Solid Earth*, **118**, 5008–5017, doi:10.1002/jgrb.50353. 39

Dobslaw, H., Bergmann-Wolf, I., Dill, R., Forootan, E., Klemann, V., Kusche, J. & Sasgen, I. (2014). *Updating ESA's Earth System Model for Gravity Mission Simulation Studies, 1. Model Description and Validation, STR 14/07*, GFZ Potsdam, Potsdam, doi:10.2312/GFZ.b103-14079. 3

Dobslaw, H., Flechtner, F., Bergmann-Wolf, I., Dahle, C., Dill, R., Esselborn, S., Sasgen, I. & Thomas, M. (2013). Simulating high-frequency atmosphere-ocean mass variability for dealiasing of satellite gravity observations: AOD1B RL05, *J. Geophys. Res.*, **118**, 3704–3711, doi:10.1002/jgrc.20271. 31, 35

Dobslaw, H. & Thomas, M. (2007). Impact of river run-off on global ocean mass redistribution, *Geophys. J. Int.*, **168**, 527–532, doi:10.1111/j.1365-246X.2006.03247.x. 32

Dong, D., Gross, R. S. & Dickey, J. O. (1996). Seasonal variations of the Earth's gravitational field: An analysis of atmospheric pressure, ocean tidal, and surface water excitation, *Geophys. Res. Lett.*, **23**, 725–728, doi:10.1029/96gl00740. 18

Drijfhout, S., Heinze, C., Latif, M. & Maier-Reimer, E. (1996). Mean circulation and internal variability in an ocean primitive equation model, *J. Phys. Oceanogr.*, **26**, 559–580, doi:10.1175/1520-0485(1996)026¡0559:mcaivi¿2.0.co;2. 31

Flechtner, F. & Dobslaw, H. (2013). Gravity Recovery and Climate Experiment AOD1B Product Description Document, **750**, 1–27. 27

Forootan, E., Bergmann-Wolf, I., Kusche, J. & Dobslaw, H. (2014). *Updating ESA's Earth System Model for Gravity Mission Simulation Studies, 3. Towards a Realistic De-Aliasing Model*, *STR 14/09*, GFZ Potsdam, Potsdam, doi:10.2312/GFZ.b103-14091. 3

Forootan, E., Didova, O., Kusche, J. & Loecher, A. (2013). Comparisons of atmospheric data and reduction methods for the analysis of satellite gravimetry observations, *J. Geophys. Res.*, **118**, 2382–2396, doi:10.1002/jgrb.50160. 22

Gruber, T., Bamber, J. L., Bierkens, M. F. P., Dobslaw, H., Murböck, M., Thomas, M., van Beek, L. P. H., van Dam, T., Vermeersen, L. L. a. & Visser, P. N. a. M. (2011). Simulation of the time-variable gravity field by means of coupled geophysical models, *Earth System Science Data*, **3**, 19–35, doi:10.5194/essd-3-19-2011. 3, 18, 20, 27, 40, 45, 46, 51, 52

Hagemann, S. & Dümenil, L. (1997). A parametrization of the lateral waterflow for the global scale, *Climate Dynamics*, **14**, 17–31, doi:10.1007/s003820050205. 39

Hughes, C. W., Tamisiea, M. E., Bingham, R. J. & Williams, J. (2012). Weighing the ocean: Using a single mooring to measure changes in the mass of the ocean, *Geophys. Res. Lett.*, **39**, L17,602, doi:10.1029/2012GL052935. 32

Klemann, V. & Martinec, Z. (2011). Contribution of glacial-isostatic adjustment to the geocenter motion, *Tectonophysics*, **511**, 99–108, doi:10.1016/j.tecto.2009.08.031. 51, 57

Kurtenbach, E., Mayer-Gürr, T. & Eicker, A. (2009). Deriving daily snapshots of the Earth's gravity field from GRACE L1B data using Kalman filtering, *Geophys. Res. Lett.*, **36**, L17,102, doi:10.1029/2009GL039564. 35

Kusche, J. (2007). Approximate decorrelation and non-isotropic smoothing of time-variable GRACE-type gravity field models, *J. Geodesy*, **81**, 733–749, doi:10.1007/s00190-007-0143-3. 13, 35

Kusche, J. (2010). Time-variable gravity field and global deformation of the Earth, in: *Handbook of Geomathematics*, edited by Freeden, W., Nashed, M. Z. & Sonar, T., Springer-Verlag, Berlin, Heidelberg, p. 253–268, doi:10.1007/978-3-642-01546-5˙8. 52

Lorbacher, K., Marsland, S. J., Church, J. a., Griffies, S. M. & Stammer, D. (2012). Rapid barotropic sea level rise from ice sheet melting, *J. Geophys. Res.*, **117**, C06,003, doi:10.1029/2011JC007733. 32

Lorenz, C. & Kunstmann, H. (2012). The hydrological cycle in three state-of-the-art reanalyses: intercomparison and performance analysis, *Journal of Hydrometeorology*, doi:dx.doi.org/10.1175/jhm-d-11-088.1. 21

Preisendorfer, R. (1988). *Principal component analysis in Meteorology and Oceanography*, Elsevier, Amsterdam, 426 p. 23

Rietbroek, R., Brunnabend, S.-E., Dahle, C., Kusche, J., Flechtner, F., Schröter, J. & Timmermann, R. (2009). Changes in total ocean mass derived from GRACE, GPS, and ocean modeling with weekly resolution, *J. Geophys. Res.*, **114**, 1–17, doi:10.1029/2009JC005449. 57

Sasgen, I., Broeke, M. v. d., Bamber, J. L., Rignot, E., Sandberg Sørensen, L., Wouters, B., Martinec, Z., Velicogna, I. & Simonsen, S. B. (2012). Timing and origin of recent regional ice-mass loss in Greenland, *Earth Planet. Sci. Lett.*, **333–334**, 293–303, doi:10.1016/j.epsl.2012.03.033. 48

Sasgen, I., Konrad, H., Ivins, E. R., Van den Broeke, M. R., Bamber, J. L., Martinec, Z. & Klemann, V. (2013). Antarctic ice-mass balance 2003 to 2012: regional reanalysis of grace satellite gravimetry measurements with improved estimate of glacial-isostatic adjustment based on gps uplift rates, *Cryosphere*, **7**, 1499–1512, doi:10.5194/tc-7-1499-2013. 48

Sørensen, L. S., Simonsen, S. B., Nielsen, K., Lucas-Picher, P., Spada, G., Adalgeirsdottir, G., Forsberg, R. & Hvidberg, C. S. (2011). Mass balance of the Greenland ice sheet (2003–2008) from ICESat data - the impact of interpolation, sampling and firn density, *Cryosphere*, **5**, 173–186, doi:10.5194/tc-5-173-2011. 46, 47

Storch, J.-S. V., Eden, C., Fast, I., Haak, H., Hernández-Deckers, D., Maier-Reimer, E., Marotzke, J. & Stammer, D. (2012). An Estimate of the Lorenz Energy Cycle for the World Ocean Based on the STORM/NCEP Simulation, *Journal of Physical Oceanography*, **42**, 2185–2205, doi:10.1175/JPO-D-12-079.1. 31

Thomas, M., Sündermann, J. & Maier-Reimer, E. (2001). Consideration of ocean tides in an OGCM and impacts on subseasonal to decadal polar motion, *Geophys. Res. Lett.*, **28**, 2457–2460, doi:10.1029/2000gl012234. 31

van den Broeke, M., Bamber, J., Ettema, J., Rignot, E., Schrama, E., van de Berg, W. J., van Meijgaard, E., Velicogna, I. & Wouters, B. (2009). Partitioning recent greenland mass loss, *Science*, **326**, 984–986, doi:10.1126/science.1178176. 48

Wang, H., Wu, P. & Wang, Z. (2006). An approach for spherical harmonic analysis of non-smooth data, *Computers & Geosciences*, **32**, 1654–1668, doi:10.1016/j.cageo.2006.03.004. 17, 18

Wolff, J. J.-O., Maier-Reimer, E. & Legutke, S. (1997). *The Hamburg ocean primitive equation model*, 13, DKRZ, 1–110 p., URL `http://mms.dkrz.de/pdf/klimadaten/models/ReportNo.13.pdf`. 31

Wunsch, C. & Stammer, D. (1997). Atmospheric Loading and the Oceanic "Inverted Barometer" Effect, *Reviews of Geophysics*, 79–107, doi:10.1029/96rg03037. 27

ISSN 1610-0956